



Residual Viscosity Stabilized RBF-FD Methods for Solving Nonlinear Conservation Laws

Igor Tominec¹ · Murtazo Nazarov¹

Received: 28 March 2022 / Revised: 23 October 2022 / Accepted: 7 November 2022 /
Published online: 4 December 2022
© The Author(s) 2022

Abstract

In this paper, we solve nonlinear conservation laws using the radial basis function generated finite difference (RBF-FD) method. Nonlinear conservation laws have solutions that entail strong discontinuities and shocks, which give rise to numerical instabilities when the solution is approximated by a numerical method. We introduce a residual-based artificial viscosity (RV) stabilization framework adjusted to the RBF-FD method, where the residual of the conservation law adaptively locates discontinuities and shocks. The RV stabilization framework is applied to the collocation RBF-FD method and the oversampled RBF-FD method. Computational tests confirm that the stabilized methods are reliable and accurate in solving scalar conservation laws and conservation law systems such as compressible Euler equations.

Keywords Nonlinear conservation law · Stabilization · Radial basis function · Finite difference · Oversampling · Residual viscosity

Mathematics Subject Classification 65M70 · 65M60

1 Introduction

We are interested in solving the following system of nonlinear conservation laws:

$$\partial_t \mathbf{U}(y, t) = -\nabla \cdot \mathbf{F}(\mathbf{U}(y, t)) \quad (y, t) \in \Omega \times \mathbb{R}^+, \quad (1)$$

with appropriate initial and boundary conditions, where $\Omega \subset \mathbb{R}^2$ is an open and bounded domain, $\mathbf{U} \in \mathbb{R}^k$ is the solution and $\mathbf{F}(\mathbf{U}) \in C^1(\mathbb{R}^k; \mathbb{R}^2)$ is a given smooth flux function. Since the flux is a nonlinear function of \mathbf{U} , the solutions of (1) lead to discontinuities and shocks in finite time. Numerical approximation of these discontinuities leads to non-physical oscillations, the so-called Gibbs phenomenon, see, e.g., Fig. 1, which make the numerical

✉ Igor Tominec
igor.tominec@it.uu.se

Murtazo Nazarov
murtazo.nazarov@it.uu.se

¹ Department of Information Technology, Division of Scientific Computing, Uppsala University, Uppsala, Sweden

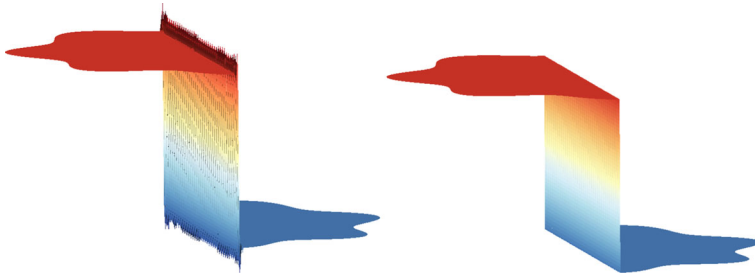


Fig. 1 A discontinuous function drawn over a star shaped domain. Left: a numerical approximation exhibiting oscillations (Gibbs phenomenon) obtained using the RBF-FD method. Right: the exact function without oscillations

scheme unstable. Therefore, adding additional stabilization terms to the scheme is vital to suppressing non-physical numerical oscillations.

State-of-the-art numerical methods for solving (1) use finite difference, finite volume, and discontinuous Galerkin approximations. One well-known approach to control and suppress the Gibbs phenomenon is the artificial viscosity method proposed by von Neumann and Richtmyer [29] in the 1950s in the context of finite difference methods. This method has been successfully used to solve many complex conservation laws, but the artificial viscosity term in [29] was not consistent with the PDE in its design.

This consistency problem was later resolved by invoking the least-squares argument in the finite element community, see, e.g., [10] and references in it. The so-called Galerkin Least Squares (GLS) method is consistent but adds artificial viscosity only in the streamline direction, which is insufficient to prove convergence. The authors of [12] proved the convergence of the GLS approximations by supplementing the method with the residual-based artificial viscosity (GLS+RV) method. The GLS+RV method is challenging to implement and requires a coupled space-time discretization. Recently in [17] we proved that the RV term is the main convergence mechanism, so we proposed to simplify the method by altogether abandoning the GLS terms. The RV method has also been used to stabilize systems of conservation laws using other discretization techniques in [15, 16, 18, 23]. Stabilization of finite element approximations only utilizing artificial viscosity conditions is not new: the well-known entropy viscosity method of Guermond et al. [9] constructs the artificial viscosity coefficient using the entropy residual of the PDE.

The aforementioned stabilization techniques have not been extended to the radial basis function (RBF) methods yet. A standard way of stabilizing hyperbolic time-dependent problems within the RBF community is to augment the collocation scheme using a hyperviscosity term that damps high-frequency oscillations [5, 7, 21, 22]. The hyperviscosity term acts on the higher derivatives of the numerical solution to establish a stable eigenvalue spectrum of the discretized advection operator. Hyperviscosity is effective in stabilizing the high-frequency mode numerical oscillations, however, as shown later in this article, for example, in Sect. 6, it is ineffective to resolve the Gibbs phenomenon resulting from the presence of shocks and discontinuities. Thus, the RBF approximation of nonlinear conservation laws requires additional shock-capturing terms. In this paper we base our stabilization approach on the artificial viscosity method, where we add an elliptic term to the RBF-FD discretization in addition to hyperviscosity. The objective of the RV stabilization is to detect the position where the shock starts to form, utilizing the magnitude of the numerical residual in (1). In the regions of Ω where the numerical solution starts to produce an overshoot over a shock, the residual

is expected to be large, whereas, in the regions where the solution is free of oscillations, the residual is expected to be small. Without loss of generality, we center our discussions on the RV stabilization, when the stabilization is augmenting an oversampled RBF-FD discretization. More traditional collocation RBF-FD schemes can be seen as a special case of oversampling. The idea can easily be applied to different RBF approximation techniques.

The paper is organized as follows. In Sect. 2 we formulate an oversampled RBF-FD method for solving a scalar conservation law, and the Euler system of equations that models compressed gas dynamics. In Sect. 3 we derive a residual viscosity stabilization in the context of the RBF-FD method, for scalar conservation laws and Euler's system of PDEs. In Sect. 4 we make a comparison between the oversampled and the collocation RBF-FD methods when solving a linear conservation law (linear advection problem) and numerically verify the RV stabilization consistency. In Sects. 5 and 6 we present numerical results for solving Burger's and the Kurganov–Petrova–Popov equations respectively. In Sect. 7 we solve several benchmark problems for the Euler equations. Final remarks are given in Sect. 8.

2 An Oversampled/Collocated RBF-FD Discretization

In this section we describe the oversampled RBF-FD discretization and the collocated RBF-FD discretization that we use to solve (1). In particular, we describe our choice of point sets spread over Ω , the formation of evaluation and differentiation matrices using the RBF-FD method, and the discretization of a time-dependent PDE where an explicit method is used to advance the solution in time.

2.1 Point Sets

The domain Ω is discretized using two point sets:

- the interpolation point set $X = \{x_i\}_{i=1}^N$ for generating the cardinal functions (left plot in Fig. 2),
- the evaluation point set $Y = \{y_j\}_{j=1}^M$ for sampling the PDE (1) (right plot in Fig. 2).

In the present work, we generate the X point set such that the mean distance between the points is set to a given value h . Depending on the application, the algorithms which we use are the 2D node generator from [6], Gmsh [8] or DistMesh [20]. The Y point set is generated by placing q points in each Voronoi region centered around every $x_i \in X$, $i = 1, \dots, N$, so that the relation between the number of X and Y points is $M \approx \lceil qN \rceil$, where we define q as the oversampling parameter. When $q = 1$ and $Y = X$, then the point sets are ready for a collocation type of discretization. When $q > 1$, then the discretization is oversampled.

2.2 Evaluation and Differentiation Matrices

We use the RBF-FD method in order to generate the RBF-FD trial space, which is spanned by a set of compactly supported cardinal basis functions $\{\Psi_i(y)\}_{i=1}^N$. These functions are constructed through a sequence of interpolation problems over stencils. An example of a stencil over Ω is given in Fig. 2.

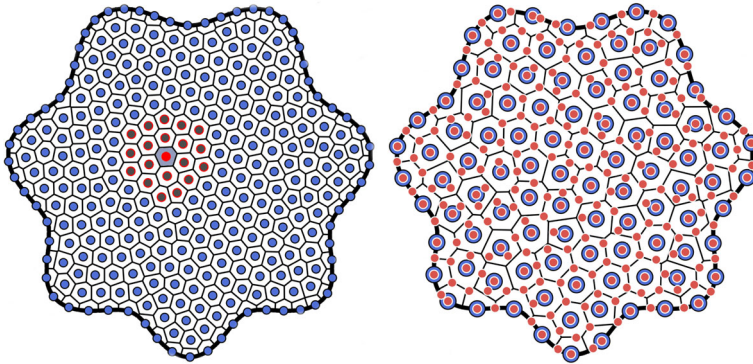


Fig. 2 Left: an example of X points (blue points with black edges) that discretize the computational domain Ω , together with one stencil (black points with a red edge) centered around the point filled with a red color. Right: an example of Y points (small red points) added on top of X points, together with a Voronoi diagram, where each cell is centered around a corresponding X point (Color figure online)

The cardinal basis functions are used to compute a PDE solution $u_h(Y, t)$ and a derivative $\mathcal{L}u_h(Y, t)$, in the form:

$$u_h(y, t) = \sum_{i=1}^N u_h(x_i, t) \Psi_i(y), \quad \mathcal{L}u_h(y, t) = \sum_{i=1}^N u_h(x_i, t) \mathcal{L}\Psi_i(y), \tag{2}$$

where \mathcal{L} is a linear differential operator and $\{u_h(x_i, t)\}_{i=1}^N$ are the solution nodal values which are the unknowns.

Using $X = \{x_i\}_{i=1}^N$, we reformulate the relations in (2) using a semi-discrete matrix notation:

$$u_h(y, t) = E(y, X)u_h(X, t), \quad u_h^{\mathcal{L}}(y, t) = D^{\mathcal{L}}(y, X)u_h(X, t). \tag{3}$$

Here $u_h(X, t) = [u_h(x_1, t), \dots, u_h(x_N, t)]^T$ is the vector of nodal values and the terms $E(y, X) = [\Psi_1(y), \dots, \Psi_N(y)]$ and $D^{\mathcal{L}}(y, X) = [\mathcal{L}\Psi_1(y), \dots, \mathcal{L}\Psi_N(y)]$ are semi-discrete matrices constructed using the RBF-FD evaluation/differentiation weights, where each set of weights is generated specifically for a point y . An algorithmic discussion on how to generate the evaluation and differentiation weights is given in [28]. A mathematical formulation for computing these weights is given in [25, 26]. In this paper we use these approaches to generate a vector of weights for every $y \in Y$, such that the weights are exact for a cubic polyharmonic spline basis and a monomial basis of degree p , which is a concept introduced in [1] and studied in [2–4, 11]. In our computations we use the stencil size $n = 2\binom{p+2}{2}$ for $p \geq 2$, and $n = 15$ for $p = 1$. To form evaluation and differentiation matrices, we sample (3) in each $y_k \in Y, k = 1, \dots, M$. This gives the following two relations:

$$u_h(Y, t) = E(Y, X)u_h(X, t), \quad u_h^{\mathcal{L}}(Y, t) = D^{\mathcal{L}}(Y, X)u_h(X, t), \tag{4}$$

where $E(Y, X)$ is a rectangular evaluation matrix of size $M \times N$ and $D^{\mathcal{L}}(Y, X)$ is a rectangular differentiation matrix of size $M \times N$. The two matrices can easily be computed in MATLAB by using the code provided in [24]. We note that when $M = N$ and $Y = X$, then the matrices are square, and the underlying discretization is of the collocation type. Otherwise, the underlying discretization is of the oversampled type.

2.3 Discretization of a Conservation Law

Here we discretize (1), where we have k unknown functions that form a set $\mathbf{U} = (u_1, u_2, \dots, u_k)$. Each unknown function in \mathbf{U} is represented using the RBF-FD ansatz (2) such that:

$$\sum_{i=1}^N \partial_t \mathbf{U}_h(x_i, t) \Psi_i(y) = - \sum_{i=1}^N F_1(\mathbf{U}_h(x_i, t)) \nabla_1 \Psi_i(y) - \sum_{i=1}^N F_2(\mathbf{U}_h(x_i, t)) \nabla_2 \Psi_i(y),$$

where $\mathbf{U}_h(x_i, t) = (u_{h,1}(x_i, t), \dots, u_{h,k}(x_i, t))$ are the i -th unknown nodal values of the functions that we are solving the conservation law for, and where we used an interpolant of the flux $F_l(\mathbf{U}_h(y, t)) = \sum_{i=1}^N F_l(\mathbf{U}_h(x_i, t)) \Psi_i(y)$, $l = 1, 2$, to compute the divergence term in (1). Now we sample the equation above in every $y \in Y$ in order to obtain a system of M equations with N unknowns:

$$\begin{aligned} \sum_{i=1}^N \partial_t \mathbf{U}_h(x_i, t) \Psi_i(y_1) &= - \sum_{i=1}^N F_1(\mathbf{U}_h(x_i, t)) \nabla_1 \Psi_i(y_1) - \sum_{i=1}^N F_2(\mathbf{U}_h(x_i, t)) \nabla_2 \Psi_i(y_1), \\ &\vdots \\ \sum_{i=1}^N \partial_t \mathbf{U}_h(x_i, t) \Psi_i(y_M) &= - \sum_{i=1}^N F_1(\mathbf{U}_h(x_i, t)) \nabla_1 \Psi_i(y_M) - \sum_{i=1}^N F_2(\mathbf{U}_h(x_i, t)) \nabla_2 \Psi_i(y_M). \end{aligned} \tag{5}$$

Matrix-vector formulations for the two problems that we consider in this paper are collected in the subsections below.

2.4 Scalar Conservation Law in a Matrix-Vector Format

Discussion in this section is kept general in the sense that it applies to \mathbf{F} for scalar conservation laws. In this case we have that $\mathbf{U}_h = u_h$ and $\mathbf{F}(u_h) = [F_1(u_h), F_2(u_h)]$. Below, we rewrite the system (5) using the matrices defined in (4) and (3):

$$E(Y, X) \partial_t u_h(X, t) = -D^{\nabla_1}(Y, X) F_1(u_h(X, t)) - D^{\nabla_2}(Y, X) F_2(u_h(X, t)). \tag{6}$$

Here $E(Y, X)$, $D^{\nabla_1}(Y, X)$ and $D^{\nabla_2}(Y, X)$ are the rectangular evaluation and differentiation matrices of size $M \times N$ defined in Sect. 2.2. The vectors F_1 and F_2 of size $M \times 1$ correspond to the components of the (non)linear flux, thus their elements are $F_{1,i}(u_h(X, t)) = F_1(u_h(x_i, t))$ and $F_{2,i}(u_h(X, t)) = F_2(u_h(x_i, t))$ respectively. Now we multiply (6) with h_y , the approximate mean distance between the Y points to arrive at:

$$\bar{E}(Y, X) \partial_t u_h(X, t) = -\bar{D}^{\nabla_1}(Y, X) F_1(u_h(X, t)) - \bar{D}^{\nabla_2}(Y, X) F_2(u_h(X, t)). \tag{7}$$

where $\bar{E}(Y, X) = h_y E(Y, X)$ and $\bar{D}(Y, X) = h_y D(Y, X)$. The multiplication by h_y is a norm scaling introduced in [26], which makes it possible to couple our discrete problem to an equivalent continuous problem [26].

When employing the oversampling approach, the system of equations (7) is rectangular and can not be solved using an explicit time-stepping technique in the form it has, as the time derivative on the left hand side is not explicitly defined. For this reason we project the residual of (7) onto the column space of $\bar{E}(Y, X)$ by multiplication with $\bar{E}^T(Y, X)$, where

for simplicity, we also drop the (Y, X) notation and obtain:

$$\bar{E}^T \bar{E} \partial_t u_h(X, t) = \bar{E}^T \left(-\bar{D}^{\nabla_1} F_1(u_h(X, t)) - \bar{D}^{\nabla_2} F_2(u_h(X, t)) \right). \tag{8}$$

Looking at (8), the components of the left hand side matrix $\bar{E}^T \bar{E}$ are:

$$(\bar{E}^T \bar{E})_{ij} = h_y^2 \sum_{k=1}^M \Psi_i(y_k) \Psi_j(y_k). \tag{9}$$

In other words, every component of $\bar{E}^T \bar{E}$ is a discrete inner product $(\Psi_i(y_k), \Psi_j(y_k))$, implying that $\bar{E}^T \bar{E}$ is a mass matrix in this inner product. The same type of inner product also applies to the components of the right-hand-side matrix products. Thus, our projection using \bar{E}^T has a tight connection with a classical Galerkin projection. A key difference is that our type of discretization uses discrete (summation) instead of a continuous (exact integration) inner product.

Now we solve (8) for the time derivative $\partial_t u_h(X, t)$ by inverting the mass matrix $\mathcal{M} = \bar{E}^T \bar{E}$, in order to get a system of ODEs ready to be advanced in time:

$$\begin{aligned} \partial_t u_h(X, t) &= \mathcal{M}^{-1} \bar{E}^T \left(-\bar{D}^{\nabla_1} F_1(u_h(X, t)) - \bar{D}^{\nabla_2} F_2(u_h(X, t)) \right) \\ &\equiv \mathcal{M}^{-1} \bar{E}^T \bar{D}(F(u_h(X, t))). \end{aligned} \tag{10}$$

To reduce the computational cost, we, instead of directly inverting \mathcal{M} , solve the system for $\partial_t u_h(X, t)$ iteratively, using the conjugate gradient method (function `pcg` () in MATLAB). Note that we have $\mathcal{M} = I$ in the collocation case, which implies that the system of equations does not have to be solved in each time step.

To (10) we also add two stabilization terms; (i) the term P_1 to stabilize the system of ODEs in time using a hyperviscosity operator, (ii) the term P_2 to treat the discontinuities which appear when using a nonlinear flux $F(u_h)$. The scheme is then:

$$\partial_t u_h(X, t) = \mathcal{M}^{-1} \left[\bar{E}^T \bar{D}(F(u_h(X, t))) + P_1 u(X, t) + P_2 u(X, t) \right]. \tag{11}$$

This is a discretization of the scalar conservation law in conservative form. In this work we formulate the hyperviscosity term $P_1 \approx \Delta^2$ as:

$$\begin{aligned} P_1 &= \gamma h_y^2 \left[D^{\Delta_{11}}(Y, X) + D^{\Delta_{22}}(Y, X) \right]^T \left[D^{\Delta_{11}}(Y, X) + D^{\Delta_{22}}(Y, X) \right] \\ \gamma &= h^{4.5}, \end{aligned} \tag{12}$$

where h_y^2 is the norm scaling and γ is the hyperviscosity scaling. Our choice of γ is justified by making the γP_1 term consistent with the PDE up to the 4-th order, and then increasing that number to 4.5 in order to allow a larger time step when using an explicit time-stepping algorithm. Term P_2 is constructed using the residual viscosity concept described in Sect. 3.

Note that when the flux $F(u_h)$ is linear, then the conservative and the non-conservative forms of a conservation laws exhibit the same numerical properties, and the ODE system (11) transforms to:

$$\partial_t u_h(X, t) = \mathcal{M}^{-1} \bar{E}^T \left(-F'_1 \bar{D}^{\nabla_1} - F'_2 \bar{D}^{\nabla_2} \right) u_h(X, t) - (P_1 + P_2) u_h(X, t) \equiv \bar{D} u_h(X, t). \tag{13}$$

Here F'_1 and F'_2 correspond to the components of the velocity field $F'(t)$. More specifically, they represent rectangular identity matrices of size $M \times N$ with components $F'_{1_{ii}} = F'_1(t)$, $F'_{2_{ii}} = F'_1(t)$, $i = 1, \dots, N$.

At this point we can use an explicit time-stepping algorithm to advance the solution of (11) from $t = 0$ to $t = T$. Throughout this paper we use the explicit classical Runge-Kutta 4 time-stepping algorithm. In the numerical experiment section of the paper we solve problems with Dirichlet-type boundary conditions on the inflow boundary. To impose these conditions we use a so-called injection method, that is, we step the discretization (11) and then in every time step overwrite the correct subset of boundary elements of $u_h(X, t)$ with the corresponding values of the Dirichlet boundary condition. After the nodal solution $u_h(X, T)$ at the final time $t = T$ is obtained, we evaluate the solution at Y points as:

$$u_h(Y, T) = E(Y, X) u_h(X, T). \tag{14}$$

2.5 System of Conservation Laws in Matrix-Vector Format: Compressible Euler Equations

Consider the compressible Euler equations in two spatial dimensions. The unknowns U and the flux $F(U)$ are in this case given by:

$$U = \begin{pmatrix} \rho \\ \mathbf{m} \\ \mathcal{E} \end{pmatrix}, \quad F(U) = \begin{pmatrix} \mathbf{m} \\ \mathbf{m} \otimes \mathbf{v} + p \mathbf{I} \\ \mathbf{v}(\mathcal{E} + p) \end{pmatrix}. \tag{15}$$

Here \mathbf{I} is an identity matrix, ρ is the density, $\mathbf{m} = (m_1, m_2)$ is the momentum, \mathcal{E} is the total energy and p is the pressure of the fluid. The relation between the momentum and the velocity field is $\mathbf{v} = \mathbf{m}/\rho$. When forming a system of equations we have 5 unknown functions, but only 4 equations. We close the system of equations using an ideal gas condition, by defining the pressure variable as: $p = \rho T = (c_{ad} - 1)(\mathcal{E} - \rho|\mathbf{v}|^2/2)$, where T is the temperature of the fluid and c_{ad} is the adiabatic gas constant. In this case the expanded form of the nonlinear conservation law (1) is:

$$\partial_t \begin{pmatrix} \rho \\ m_1 \\ m_2 \\ \mathcal{E} \end{pmatrix} = \begin{pmatrix} -\nabla_1 m_1 - \nabla_2 m_2 \\ -\nabla_1(m_1 v_1) - \nabla_2(m_2 v_1) - \nabla_1 p \\ -\nabla_1(m_1 v_2) - \nabla_2(m_2 v_2) - \nabla_2 p \\ -\nabla_1(v_1(\mathcal{E} + p)) - \nabla_2(v_2(\mathcal{E} + p)) \end{pmatrix}. \tag{16}$$

We discretize the above system by introducing unknown nodal values for all unknown functions $\rho(X, t), m_1(X, t), m_2(X, t), E(X, t)$. The oversampled RBF-FD discretization analogous to (11) is then:

$$\partial_t \begin{pmatrix} \rho(X, t) \\ m_1(X, t) \\ m_2(X, t) \\ \mathcal{E}(X, t) \end{pmatrix} = \mathcal{M}^{-1} \begin{pmatrix} E^T G_\rho(Y, t) + P \rho(X, t) \\ E^T G_{m_1}(Y, t) + P m_1(X, t) \\ E^T G_{m_2}(Y, t) + P m_2(X, t) \\ E^T G_\mathcal{E}(Y, t) + P \mathcal{E}(X, t) \end{pmatrix}, \tag{17}$$

where:

$$\begin{aligned} G_\rho(Y, t) &= -D^{\nabla_1} m_1(X, t) - D^{\nabla_2} m_2(X, t), \\ G_{m_1}(Y, t) &= -D^{\nabla_1}(m_1(X, t) v_1(X, t)) - D^{\nabla_2}(m_2(X, t) v_1(X, t)) - D^{\nabla_1} p, \\ G_{m_2}(Y, t) &= -D^{\nabla_1}(m_1(X, t) v_2(X, t)) - D^{\nabla_2}(m_2(X, t) v_2(X, t)) - D^{\nabla_2} p, \\ G_\mathcal{E}(Y, t) &= -D^{\nabla_1}(v_1(\mathcal{E} + p)) - D^{\nabla_2}(v_2(\mathcal{E} + p)), \\ P &= -P_1 - P_2, \end{aligned} \tag{18}$$

with differentiation matrices $D^{\nabla_1}, D^{\nabla_2}$ defined in Sect. 2.2, and stabilizers P_1 and P_2 described in Sect. 2.4. The Dirichlet-type boundary conditions for a given unknown function are imposed using the injection method, just as described for the scalar conservation law in Sect. 2.4. After the system of ODEs is advanced to the final time $t = T$, each unknown set of nodal values is evaluated at the Y points, analogously to (14).

3 Residual Based Artificial Viscosity Stabilization of Shocks for Nonlinear Conservation Laws

Solutions to nonlinear conservation laws (1) are discontinuous, when the flux $F(U)$ does not include any physical viscous forces. Numerical approximation of discontinuous functions suffers from the Gibbs phenomenon. Based on [17–19] we formulate a residual based viscosity stabilization of the solution in the context of the RBF-FD method.

The numerical scheme is stabilized using a viscosity term $P_2 \approx \nabla \cdot (\varepsilon \nabla u)$, where ε is a spatially variable coefficient, computed such that the viscous term is prevalently active in the regions of discontinuities. The viscosity term is below discretized by using the differentiation matrices introduced in Sect. 2.2:

$$P_2 = (D^{\nabla_1})^T \text{diag}(E \varepsilon(X, t_n)) D^{\nabla_1} + (D^{\nabla_2})^T \text{diag}(E \varepsilon(X, t_n)) D^{\nabla_2}. \tag{19}$$

The definition of ε for scalar conservation laws and the Euler system, is given in the following two subsections.

3.1 Definition of the Viscosity Coefficient for Scalar Conservation Laws

The discrete problem which we aim to stabilize is (11). The discussion is centered around the stabilization term P_2 defined in (19). For each node $x_i \in X, i = 1, \dots, N$, we define the viscosity coefficient vector ε included inside the definition of P_2 as:

$$\begin{aligned} \varepsilon(x_i, t_n) &= \min(\varepsilon_{RV}(x_i, t_n), \varepsilon_{UW}(x_i, t_n)), \quad n = 2, 3, \dots, \\ \varepsilon(x_i, t_n) &= \varepsilon_{UW}(x_i, t_n), \quad n = 1. \end{aligned} \tag{20}$$

Here ε_{RV} and ε_{UW} are the residual and the upwind coefficients respectively. Let K_i be a Voronoi cell with a corresponding Voronoi center x_i , and $y_j \in Y$ an evaluation point (see the right plot in Fig. 2). Then the definitions of ε_{RV} and ε_{UW} are [17]:

$$\begin{aligned} \varepsilon_{RV}(x_i, t_n) &= C_{RV} h_{loc}^2(x_i) \max_{y_j \in K_i} |R(y_j, t_n)| \frac{1}{n(x_i)}, \\ \varepsilon_{UW}(x_i, t_n) &= \frac{1}{2} h_{loc}(x_i) \max_{y_j \in K_i} \sqrt{F'_1(u_h(y_j, t_n))^2 + F'_2(u_h(y_j, t_n))^2}. \end{aligned} \tag{21}$$

Here we define $h_{loc}(x_i)$ as the minimum pairwise distance between points in a patch centered around x_i , where the patch consists of 5 points closest to x_i [23]. The temporal solution $u_h(y_j, t_n)$ at a point $y_j \in Y$ comes from the relation $u_h(Y, t_n) = E(Y, X) u_h(X, t_n)$. The user-defined constant C_{RV} is of size $\mathcal{O}(1)$ and is independent of $h_{loc}(x_i)$. As $C_{RV} \rightarrow \infty$, then $\varepsilon_{RV} \rightarrow \infty$, and $\varepsilon \rightarrow \varepsilon_{UW}$. On the other hand, as $C_{RV} \rightarrow 0$, then $\varepsilon_{RV} \rightarrow 0$, and $\varepsilon \rightarrow 0$.

The term $n(x_i, t_n)$ is the residual normalization defined by:

$$n(x_i, t_n) = \left| u_{\text{loc}} - \|u_h(X, t_n) - \bar{u}_h(X, t_n)\|_{\infty} \right|, \tag{22}$$

$$u_{\text{loc}} = \max_{y_j \in K_i} u_h(y_j, t_n) - \min_{y_j \in K_i} u_h(y_j, t_n),$$

where $\bar{u}_h(X, t_n)$ is the mean of the temporal solution $u_h(X, t_n)$. The role of the normalization is to unify the physical units of ε_{RV} and ε_{UW} . The residual $R(Y, t_n)$ is defined as:

$$R(Y, t_n) = E \left(D^{\partial t} u_h(X, t_n) \right) + D^{\nabla 1} F_1(u_h(X, t_n)) + D^{\nabla 2} F_2(u_h(X, t_n)), \tag{23}$$

where $D^{\nabla 1} F_1(u_h(X, t_n)) + D^{\nabla 2} F_2(u_h(X, t_n))$ is the flux divergence of the solution at time t_n computed using the RBF-FD differentiation matrices introduced in Sect. 2.2. Furthermore, E is an evaluation matrix also introduced in Sect. 2.2, and the term $D^{\partial t} u_h(X, t_n)$ is an approximation of the time derivative at t_n using the already computed solution from previous time points $t_n, t_{n-1}, t_{n-2}, \dots$. We construct $D^{\partial t}$ in two different ways: (i) when the solution is advanced in time using a constant Δt we use the backward-differentiation formulae (BDF), (ii) when the solution is advanced in time by a variable $\Delta t_i, i = 1, 2, \dots$, then we construct an approximation to a time derivative using the polynomial basis, in each time step. At the beginning of the simulation we can only use a few points from the past temporal solutions. When a sufficient amount of temporal solutions have been computed we are allowed to use a high-order formula. We then write that:

$$D^{\partial t} |_{t_n} = \begin{cases} D_1^{\partial t} & n = 2, \\ D_2^{\partial t} & n = 3, \\ D_3^{\partial t} & n = 4, \\ D_4^{\partial t} & n \geq 5, \end{cases} \tag{24}$$

where $D_1^{\partial t}$ is a differentiation operator of order 1, $D_2^{\partial t}$ of order two, and so on. In the case (i) we use the BDF4 formula to define $D_{\bar{k}}^{\partial t}$, for $\bar{k} = 1, \dots, 4$ consecutively as:

$$D_1^{\partial t} u_h(X, t_n) = \frac{1}{\Delta t} \left(u_h(X, t_n) - u_h(X, t_{n-1}) \right),$$

$$D_2^{\partial t} u_h(X, t_n) = \frac{1}{\Delta t} \frac{3}{2} \left(u_h(X, t_n) - \frac{4}{3} u_h(X, t_{n-1}) + \frac{1}{3} u_h(X, t_{n-2}) \right),$$

$$D_3^{\partial t} u_h(X, t_n) = \frac{1}{\Delta t} \frac{11}{6} \left(u_h(X, t_n) - \frac{18}{11} u_h(X, t_{n-1}) + \frac{9}{11} u_h(X, t_{n-2}) - \frac{2}{11} u_h(X, t_{n-3}) \right),$$

$$D_4^{\partial t} u_h(X, t_n) = \frac{1}{\Delta t} \frac{25}{12} \left(u_h(X, t_n) - \frac{48}{25} u_h(X, t_{n-1}) + \frac{36}{25} u_h(X, t_{n-2}) - \frac{16}{25} u_h(X, t_{n-3}) + \frac{3}{25} u_h(X, t_{n-4}) \right). \tag{25}$$

In the case (ii) we construct $D_{\bar{k}}^{\partial t}, \bar{k} = 1, \dots, 4$ by computing a set of differentiation weights through a 1D polynomial interpolant $u(t) = \sum_{j=1}^{\bar{k}+1} \xi_i t^{j-1}$, where $\bar{k} + 1$ is the number of the time points in which we already know the solution $u(t_1), u(t_2), \dots, u(t_{\bar{k}+1})$, and \bar{k} is the desired order of the approximation. Then we sample $u(t)$ in $t_n, \dots, t_{n-\bar{k}}$ to obtain a system of equations $\underline{u} = A \underline{\xi}$, where $A_{ij} = t_i^{j-1}$ and $\xi_i, j = 1, \dots, \bar{k} + 1, i = 1, \dots, \bar{k} + 1$ are the

interpolation matrix and the unknown coefficients respectively. A time-derivative of $u(t)$ is $\partial_t u(t) = \sum_{j=1}^{k+1} (j-1)t^{j-2} \xi_j$, an equivalent vector formulation is $\partial_t u(t) = \underline{b}(t) \underline{\xi}$, where $b_j(t) = (j-1)t^{j-2}$. Plugging the computed $\underline{\xi}$ into $\partial_t u(t)$ we have $\partial_t u(t) = \underline{b}(t) A^{-1} \underline{u} \equiv \underline{w}(t) \underline{u}$. Here $\underline{w}(t)$ is a final vector of $k+1$ weights for computing a derivative in time when the time grid is non-uniform. The MATLAB code to compute \underline{w} is provided in Appendix 1.

Note that the time derivative approximated using the approaches (i) and (ii), is used only with the purpose to compute the residual, once the solution at t_n has already been computed. The time stepping scheme that is actually advancing the solution in time is chosen differently.

Remark 1 (Computation of residual) Note that the order of accuracy of the flux derivatives in the residual computation (23) is $\mathcal{O}(h^p)$, where p is the polynomial degree used to construct the stencil based approximation. The accuracy of the time derivative approximation when computing the residual can be at least of order $\mathcal{O}(h^{p-2})$. The total residual will then be of order $\mathcal{O}(h^{p-2})$. Then the coefficient \uparrow_{RV} in (21) is of the order $\mathcal{O}(h^p)$, since the factor h^2_{loc} is multiplying the residual. In practice, we suggest using different orders of approximation of the derivatives in time and space when computing the residual. This gives a larger residual discrepancy, resulting in more viscosity, and, therefore, more robust scheme.

3.2 Definition of the Viscosity Coefficient for the Euler System

Here we formulate the viscosity coefficient ε for the Euler system of equations (17). The ε coefficient is computed using the same relation as in (20), however, the definitions of ε_{UW} and ε_{RV} in (20) are different. The upwind viscosity coefficient at time t_n and a point $x_i \in X$ is defined as:

$$\varepsilon_{UW}(x_i, t_n) = \frac{1}{2} h_{loc}(x_i) \left(\sqrt{v_1^2(x_i, t_n) + v_2^2(x_i, t_n)} + \sqrt{c_{ad} T(x_i, t_n)} \right), \tag{26}$$

where the term in parenthesis is the local wave speed computed from the eigenvalues of $\frac{\partial \underline{F}}{\partial \underline{U}}$, and where $v_1(x_i, t_n) = m_1(x_i, t_n)/\rho(x_i, t_n)$, $v_2(x_i, t_n) = m_2(x_i, t_n)/\rho(x_i, t_n)$ are the velocities in horizontal and vertical directions respectively, and $T = p(x_i, t)/\rho(x_i, t)$ is the temperature of the fluid, and the internodal distance $h_{loc}(x_i)$ is defined in the scope of (21). The coefficient ε_{RV} is defined by:

$$\varepsilon_{RV}(x_i, t_n) = C_{RV} h^2_{loc}(x_i) \max \left(\frac{|R_\rho|}{n_\rho}, \frac{|R_{m_1}|}{n_{m_1}}, \frac{|R_{m_2}|}{n_{m_2}}, \frac{|R_\mathcal{E}|}{n_\mathcal{E}} \right), \tag{27}$$

where the residuals R_* are defined for each equation in (17), analogously to the formulation for the scalar conservation law in (23). We have:

$$\begin{aligned} R_\rho(Y, t_n) &= E \left(D_{BDF}^{\partial_t} \rho(X, t_n) \right) - G_\rho(Y, t_n), \\ R_{m_1}(Y, t_n) &= E \left(D_{BDF}^{\partial_t} m_1(X, t_n) \right) - G_{m_1}(Y, t_n), \\ R_{m_2}(Y, t_n) &= E \left(D_{BDF}^{\partial_t} m_2(X, t_n) \right) - G_{m_2}(Y, t_n), \\ R_\mathcal{E}(Y, t_n) &= E \left(D_{BDF}^{\partial_t} \mathcal{E}(X, t_n) \right) - G_\mathcal{E}(Y, t_n). \end{aligned} \tag{28}$$

Here G_ρ, G_{m_1}, G_{m_2} and $G_\mathcal{E}$ are defined in (18), and the time derivative approximation $D_{BDF}^{\partial_t}$ is the same as defined in (24) and (25). Each normalization n_* in (27) follows the same

definition as in (22). For example, n_ρ is defined as:

$$n_\rho(x_i, t_n) = \left| \rho_{\text{loc}} - \|\rho(X, t_n) - \bar{\rho}(X, t_n)\|_\infty \right|, \tag{29}$$

$$\rho_{\text{loc}} = \max_{y_j \in K_i} \rho(y_j, t_n) - \min_{y_j \in K_i} \rho(y_j, t_n), \quad i = 1, \dots, N,$$

where $\bar{\rho}(X, t_n)$ is the mean density at $t = t_n$ and K_i is a Voronoi cell centered around $x_i \in X$.

4 Numerical Study I: Linear Advection Problem

Throughout this section we compare collocation and oversampled RBF-FD methods, and investigate how do the hyperviscosity term (12) and the residual viscosity term (19) influence the numerical solution. Consider F is a linear flux with time-dependent velocity field given by:

$$F'(u) = F' = (\cos(2\pi t), \sin(2\pi t)). \tag{30}$$

The boundary of Ω is defined using polar coordinates (r, θ) , where: $r = 1 + \frac{1}{10}(\sin(7\theta) + \sin(\theta))$ for $\theta \in [0, 2\pi]$. We use the explicit classical Runge-Kutta 4 method to advance the solution in time. The constant time step is chosen as:

$$\Delta t = \text{CFL} \min_{x_i \in X} \frac{h_{\text{loc}}(x_i)}{\sqrt{(F'_1(t))^2 + (F'_2(t))^2}} = \text{CFL} \min_{x_i \in X} h_{\text{loc}}(x_i), \tag{31}$$

where we also used that $(F'_1(t))^2 + (F'_2(t))^2 = 1$, since F' is in (30) chosen as the rotational velocity field. The term $h_{\text{loc}}(x_i)$ is defined in the scope of (21). The constant CFL is the Courant-Friedrichs-Lax number, specified in each subsection separately. The relative approximation errors in 2- and 1-norm at final time $t = T$ are computed as:

$$\|e\|_2 = \frac{\|E(Y, X) u_h(X, T) - u(Y, T)\|_2}{\|u(Y, T)\|_2}, \quad \|e\|_1 = \frac{\|E(Y, X) u_h(X, T) - u(Y, T)\|_1}{\|u(Y, T)\|_1}, \tag{32}$$

where $u(Y, T)$ is the exact solution at $t = T$, sampled at Y points.

4.1 Smooth Initial Condition: Approximation Error and Stability Properties

Oversampled methods are normally associated with improved stability properties. In this section we investigate whether this is also true when solving hyperbolic problems, i.e., if there is a positive effect of oversampling on the eigenvalue spectrum of the discretized advection operator.

Provided that $d = d(y_1, y_2) = \sqrt{(y_1 - 0.2)^2 + (y_2 - 0.2)^2}$, the initial condition at $t = 0$ is a C^6 compactly supported Wendland function centered in a point $(0.2, 0.2)$:

$$u(y, 0) = \begin{cases} (1 - d)^6 (35d^2 + 18d + 3), & d \leq 0.4 \\ 0, & \text{otherwise.} \end{cases} \tag{33}$$

The initial condition is plotted in Fig. 3.

The discretized advection operator D is given in (13). In this section we only want to observe the effect of oversampling on the time stability of the discretization, and compare

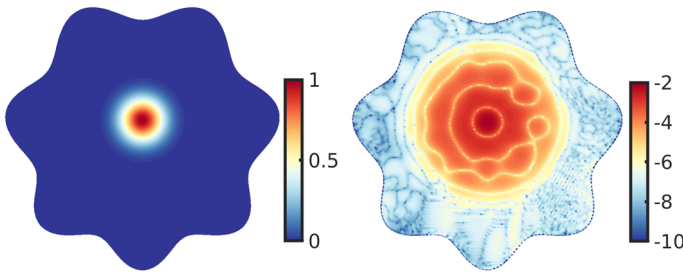


Fig. 3 Linear advection of a compactly supported C^6 function using a rotational velocity field. Initial condition is given in the left image. The spatial error distribution in the \log_{10} scale, after the initial condition is rotated five times, and an oversampled RBF-FD method is in time stabilized using hyperviscosity, is given in the image on the right. Method parameters are set to $h = 0.03$ and $p = 4$ and $q = 5$

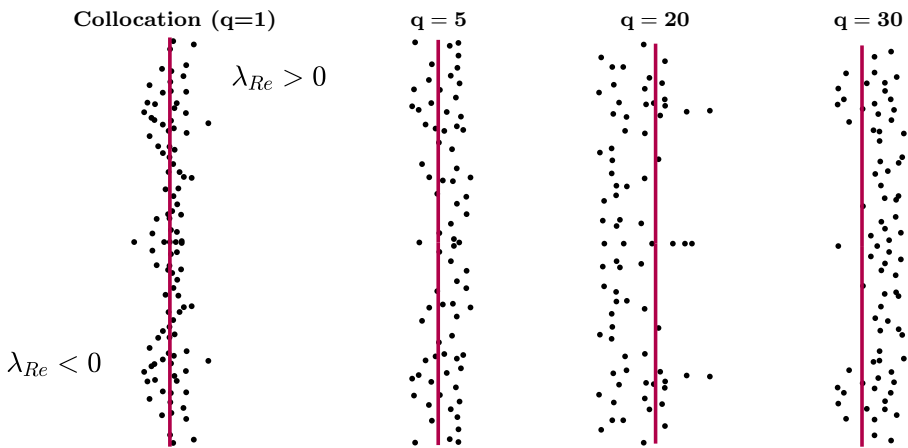


Fig. 4 Linear advection of a compactly supported C^6 function using a rotational velocity field: a close-up of the eigenvalue spectra for different choices of the oversampling parameter q , when none of the cases is stabilized using hyperviscosity. Eigenvalues left of the red line have a negative real part, while the eigenvalues on the right of the red line have a positive real part (Color figure online)

the results to the collocation case. The test case does not involve any shocks, therefore, we set $P_2 = 0$. When studying eigenvalues, we enforce zero Dirichlet boundary condition exactly in D , by removing all rows and columns corresponding to the boundary unknowns. In Fig. 4 we display a close up of the eigenvalue spectrum around the imaginary axis, when the discretization is not stabilized, that is, when the parameter γ in P_1 included into (13) is set to 0. We observe that the spectrum of the collocation RBF-FD method includes eigenvalues with a positive real part. These eigenvalues cause spurious growth when the solution is advanced in time. However, the situation is not improved as we introduce an oversampled discretization: for the oversampling parameters $q = 5$, $q = 20$ and $q = 30$, the eigenvalue spectra still include eigenvalues with a positive real part. We do not observe that the positive real part is asymptotically shifted towards the negative imaginary half-plane, as q is increased. Our conclusion is that oversampling by itself does not stabilize the eigenvalue spectrum of the semi-discrete PDE problem when the RBF-FD method is used.

Next, we study the eigenvalue spectra when hyperviscosity is added to (13), that is, when the parameter γ and the second-order hyperviscosity P_1 follow the definition in (12). The

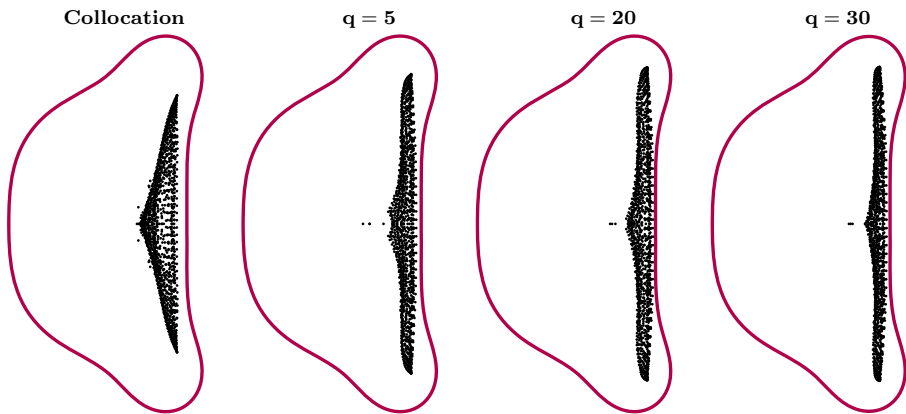


Fig. 5 Linear advection of a compactly supported C^6 function using a rotational velocity field: eigenvalue spectra for different choices of the oversampling parameter q , when the discretizations are stabilized in time using the hyperviscosity term. The closed red line represents stability region of the Runge-Kutta 4 method for advancing the system of ODEs in time (Color figure online)

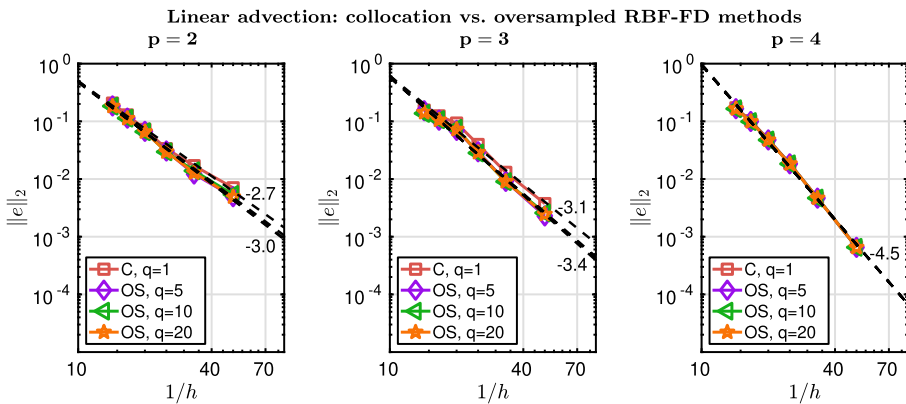


Fig. 6 Linear advection of a compactly supported C^6 function using a rotational velocity field: convergence as a function of the inverse internodal distance $1/h$. Experiments in each plot correspond to using a different degree of monomial basis p used to construct the RBF-FD trial space. Within each plot, different oversampling parameters q are used to oversample (OS) the semi-discrete system of ODEs. The case $q = 1$ represents the collocation RBF-FD method, and other choices of q represent the oversampled RBF-FD method

results are given in Fig. 5, where we observe that the eigenvalue spectra are stabilized. The eigenvalue distributions are similar across the different methods.

Now we compare the hyperviscosity stabilized collocation and oversampled RBF-FD methods in terms of the approximation error when the internodal distance h is decreased ($1/h$ increased). The simulation is run until $t = 5$. In this time the initial condition makes five full rotations around the point $(0, 0)$. To determine the time step we use $CFL = 0.2$. Convergence results are collected in Fig. 6.

For all tested degrees of the appended monomial bases, we observe that the errors are very similar in magnitude and convergence trend, for both collocation and oversampled RBF-FD methods. An increase in the oversampling parameter does not lead to a better accuracy in this case. This conclusion is in line with the results on solving elliptic PDEs with pure Dirichlet

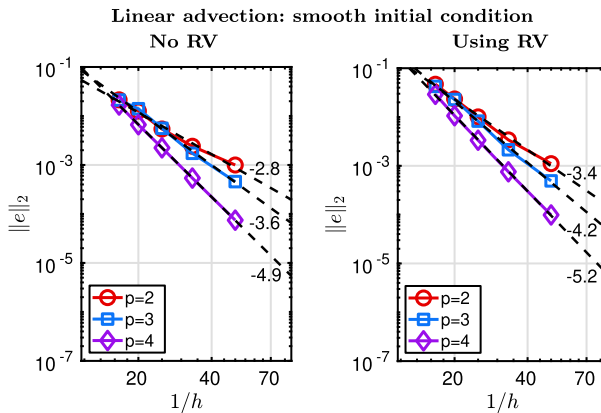


Fig. 7 Linear advection of a compactly supported C^6 function using a rotational velocity field: convergence as a function of the inverse internodal distance $1/h$, for an oversampled RBF-FD method ($q = 5$). The CFL number is set to 0.2, the initial condition is rotated until time $t = 1$

boundary conditions, presented in [26]. An example of a spatial error distribution after five revolutions of the initial condition is displayed in Fig. 3.

4.2 Smooth Initial Condition: A Residual Viscosity Test

We again use (30) as the velocity field and a compactly supported C^6 Wendland function (33) as the initial condition. The difference compared with the previous experiment is that we now activate the residual viscosity (RV) term P_2 in our discretization (13). The objective is to check if P_2 distorts high-order convergence when the solution is smooth. We use $C_{RV} = 1$ as the scaling used in (21). We use $CFL = 0.5$ and run our simulation until $t = 1$. The results are collected in Fig. 7.

We observe that the approximation error is slightly larger throughout the refinement of h when RV is used. However, the convergence trend when RV is used does not change significantly compared with the case when RV is not used. This is accounted to the fact that the residual is small when no discontinuity is present in the numerical solution. Since the coefficient ε given in (20) that scales P_2 in (19) is residual dependent, the viscosity terms plays a negligible role in the numerical discretization given in (13). An important outcome of this subsection is that the residual viscosity can be used in cases when we do not know whether the solution is going to develop a shock, without sacrificing the order of convergence before the shock is developed.

4.3 Discontinuous Initial Condition: A Residual Viscosity Test

Now we again consider a linear advection problem with (30) as the velocity field, but use a discontinuous initial condition; a cylinder with radius 0.3, cut from two sides, given in Fig. 8. We let the initial condition rotate around its axis one time (until $t = 1$) when $h = 0.01$, $p = 4$, and compare three scenarios:

1. Residual viscosity is not active: in (19) we set $\varepsilon = 0$.

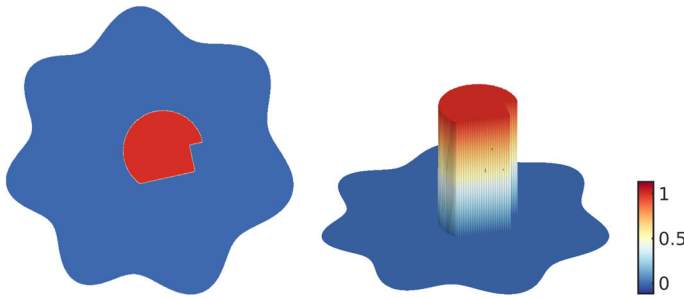


Fig. 8 Linear advection of a discontinuous initial condition: exact solutions at $t = 1$, drawn from two perspectives

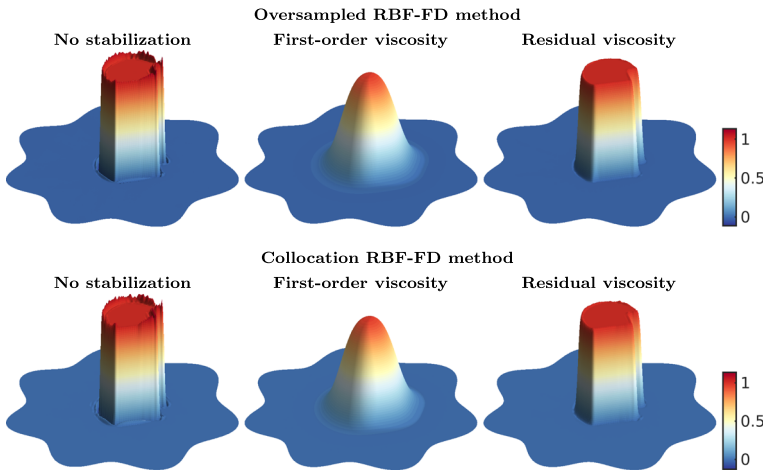


Fig. 9 Linear advection of a discontinuous initial condition when different stabilization techniques are used, side view. All solutions are displayed after one rotation at $t = 1$. Parameters used were $h = 0.01$, $p = 4$, $q = 5$. The CFL condition when first-order viscosity was set to 0.1, and to 0.5 in cases when residual viscosity method was used and when no stabilization was used

2. Only the first order viscosity is active: instead of following the definition of ε in (20) we set $\varepsilon = \varepsilon_{UV}$ throughout Ω .
3. Residual viscosity is active: ε is taken as defined in (20).

Note that the hyperviscosity term P_1 is essential to stabilize the discretization in time and is active in all three scenarios. We use $CFL = 0.1$ when using first-order viscosity and $CFL = 0.5$ when using RV and when not stabilizing discontinuities. We use $C_{RV} = 1$ as the scaling used in (21). Results for the collocation RBF-FD method and an oversampled RBF-FD method are given in Fig. 9 (side view).

From the two figures we observe that the numerical scheme without stabilization induces oscillations (Gibbs phenomenon) around the discontinuity. This is expected. When the numerical scheme is stabilized by the first-order viscosity term, we observe that the initial condition is highly smeared, to the extent where it is difficult to recognize the characteristic shape of the initial condition. The main observation is that after the oversampled RBF-FD method is stabilized using the residual viscosity term, the oscillations are significantly damped, while the initial condition kept its characteristic shape throughout the simulation. We observe that

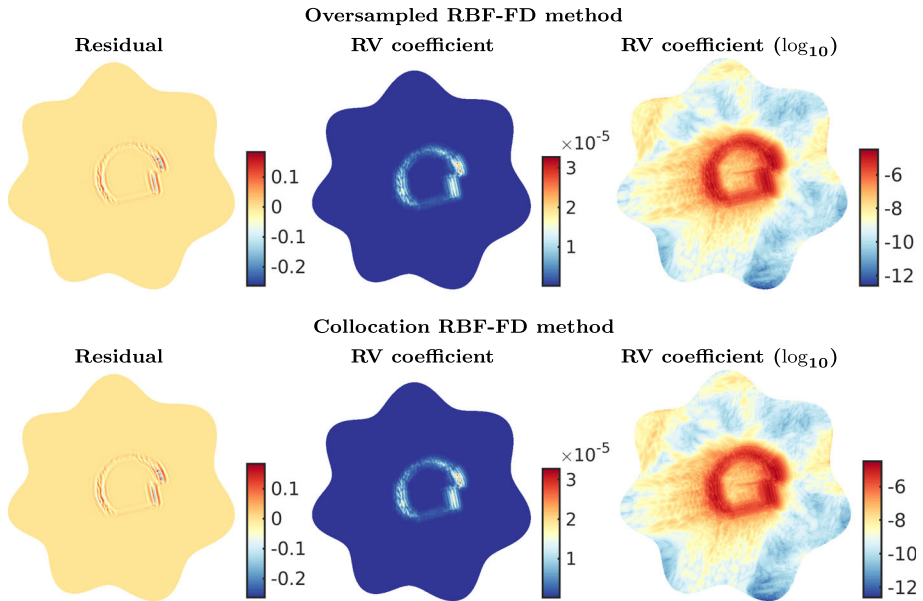


Fig. 10 Linear advection of a discontinuous initial condition when residual viscosity is used. The pictures show the residual and the residual-viscosity (RV) coefficients in linear and logarithmic scale

the RV solution is not significantly different compared with the RV solution when an oversampled RBF-FD method is used. It is however possible to observe a few more oscillations on the outer edge of the slotted cylinder, when the collocation RBF-FD method is used.

The effectiveness of the residual viscosity method when an oversampled RBF-FD method is used, is displayed in Fig. 10, where we show the spatial distribution of the residual (23) and the coefficient ε given in (20). We observe that the residual is giving the information about the position of the discontinuity (large oscillations) present in the solution. This makes the residual viscosity coefficient ε (defined in (20) and (21)) large in the region of the shock, but small away from the shock. The results for the oversampled and the collocation RBF-FD methods are—in the “eyeball norm”—identical.

We conclude that for the cases considered in this subsection, the residual viscosity approach detects discontinuities in an accurate way, for both RBF-FD methods that we tested. In this paper we are mainly interested in the performance of the oversampled RBF-FD method, which we now focus on in the results below.

In Fig. 11 we provide convergence results for the oversampled RBF-FD method, for different choices of p , when the numerical scheme includes: (i) no stabilization, (ii) first-order viscosity, (iii) residual-viscosity. The CFL numbers used for the simulation were 0.2 for cases (i) and (ii), and 0.1 for case (iii). The observed convergence rates in all cases are what we expect, since the solution is discontinuous and the error is measured in 2-norm. The approximation error is smallest in the case where no shock stabilization is added. This can be accounted to an observation made in Fig. 9, where oscillations when no shock stabilization was added were not as severe as one expected. However, we do expect the oscillations to become significantly larger when the flux $F(u)$ becomes nonlinear with respect to u (studied in later sections). Additional experiments revealed that the approximation error in ∞ -norm does not converge, which is expected.

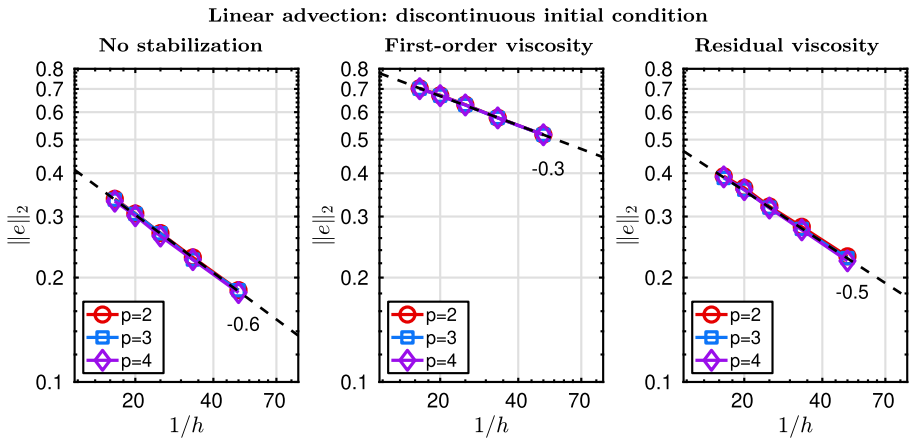


Fig. 11 Linear advection of a discontinuous initial condition, convergence study of the approximation error under node refinement, for different degrees p of the monomial basis used to construct the interpolation problem over a stencil. The three plots show cases when numerical scheme includes: **i** no shock stabilization, **ii** first-order viscosity stabilization, **iii** residual-viscosity stabilization

5 Numerical Study II: Burger’s Equation

In this section we solve Burger’s equation in two dimensions. The flux is given by $F(u) = (\frac{u^2}{2}, \frac{u^2}{2})$, and the velocity field by $F'(u) = (u, u)$. The exact solution to the considered problem is:

$$u(y, t) = \begin{cases} \begin{cases} -0.2 & \text{if } y_1 < \frac{1}{2} - \frac{3t}{5} \text{ and } \begin{cases} y_2 > \frac{1}{2} + \frac{3t}{20}, \\ \text{otherwise,} \end{cases} \\ 0.5 & \end{cases} \\ \begin{cases} -1 & \text{if } \frac{1}{2} - \frac{3t}{5} < y_1 < \frac{1}{2} - \frac{t}{4} \text{ and } \begin{cases} y_2 > -\frac{8y_1}{7} + \frac{15}{14} - \frac{15t}{28}, \\ \text{otherwise,} \end{cases} \\ 0.5 & \end{cases} \\ \begin{cases} -1 & \text{if } \frac{1}{2} - \frac{t}{4} < y_1 < \frac{1}{2} + \frac{t}{2} \text{ and } \begin{cases} y_2 > \frac{y_1}{6} + \frac{5}{12} - \frac{5t}{24}, \\ \text{otherwise,} \end{cases} \\ 0.5 & \end{cases} \\ \begin{cases} -1 & \text{if } \frac{1}{2} + \frac{t}{2} < y_1 < \frac{1}{2} + \frac{4t}{5} \text{ and } \begin{cases} y_2 > y_1 - \frac{5}{18t} (y_1 + t - \frac{1}{2})^2, \\ \text{otherwise,} \end{cases} \\ \frac{2y_1-1}{2t} & \end{cases} \\ \begin{cases} -1 & \text{if } y_1 > \frac{1}{2} + \frac{4t}{5} \text{ and } \begin{cases} y_2 > \frac{1}{2} - \frac{t}{10}, \\ \text{otherwise.} \end{cases} \\ 0.8 & \end{cases} \end{cases} \tag{34}$$

The initial condition simplifies to:

$$u(y, 0) = \begin{cases} -0.2, & \text{if } y_1 < 0.5 \text{ and } y_2 > 0.5, \\ -1, & \text{if } y_1 > 0.5 \text{ and } y_2 > 0.5, \\ 0.5, & \text{if } y_1 < 0.5 \text{ and } y_2 < 0.5, \\ 0.8, & \text{if } y_1 > 0.5 \text{ and } y_2 < 0.5. \end{cases} \tag{35}$$

The initial condition and the exact solution to the considered problem are visualized in Fig. 12.

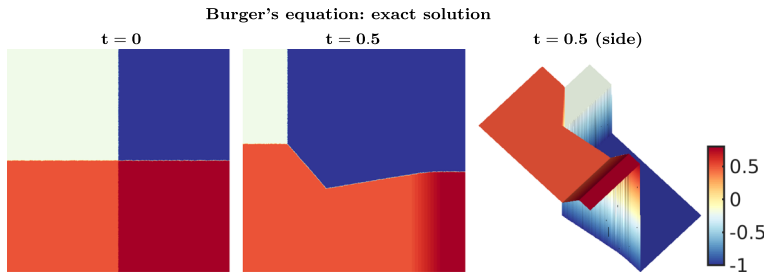


Fig. 12 Exact solution to the considered Burger's equation, at time $t = 0$ (initial condition, and at time $t = 0.5$ from two visual perspectives

A variable time step is chosen as:

$$\Delta t = \text{CFL} \min_{x_i \in X} \left[\frac{h_{\text{loc}}(x_i)}{\sqrt{(F'_1(u(x_i, t)))^2 + (F'_2(u(x_i, t)))^2}} \right], \tag{36}$$

where $h_{\text{loc}}(x_i)$ is defined in the scope of (21).

We solve this problem on a unit square $\Omega = [0, 1] \times [0, 1]$ until $t = 0.5$ and use Dirichlet boundary conditions with the data obtained from the exact solution. Our objective is to make observations on how the oversampled RBF-FD method behaves when the nonlinear flux $F(u)$ is inducing shocks in the solution. We focus on cases when we stabilize the Gibbs phenomenon through P_2 defined in (19) using: (i) first order viscosity (we override (20) by $\varepsilon = \varepsilon_{\text{UW}}$), (ii) residual viscosity (ε as defined in (20)). The hyperviscosity term (12) is always added to the numerical scheme for the purposes of stabilization in time. Throughout this section we use an oversampling parameter $q = 5$ and the CFL number 0.2. The nodes in X point set are generated using the algorithm presented in [6].

First, we examine the numerical solution from a visual perspective in the three cases: when the RBF-FD method is not shock-stabilized, when the method is stabilized with the first-order viscosity and when the method is stabilized using the residual viscosity method. The parameters that we use are $h = 0.005$ ($N = 40000$), $p = 3$ and $q = 5$. The numerical solution is a subject to rapid exponential growth when the Gibbs phenomenon is not stabilized with any of the approaches, and we therefore can not provide any visual results. The solution when the numerical scheme is stabilized using first order viscosity and residual viscosity, is given in Figs. 13 and 14.

In all cases where we attempted to stabilize the solution, the numerical solution was stable at the end. The smoothest solution is expectedly the one where the first-order viscosity is active throughout Ω . When RV is used, the details around the discontinuities are preserved in a better way compared with the first-order viscosity solution. The RV solution when c_{RV} in (21) is set to 1 is more oscillatory compared with the RV solution when c_{RV} is set to 4. Despite the oscillations, the important outcome is that the solution is stable in both cases. Here we point out that these solutions are computed on scattered points. We made the same tests on Cartesian points, where we noticed that the oscillations were smaller.

In Fig. 15 we display the spatial variation of the viscosity coefficient ε defined in (20), for cases when the first-order viscosity is used and when RV is used. We see that the viscosity coefficient is large only in the vicinity of the shock, when RV is used, thus, the shocks are well captured.

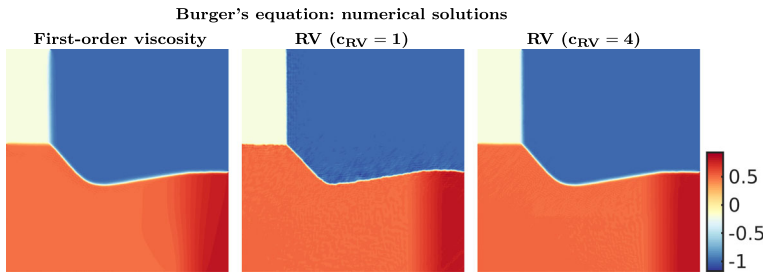


Fig. 13 Numerical solutions to the Burger’s equations, when the oversampled RBF-FD discretization is shock-stabilized using first-order viscosity, and residual viscosity for two choices of constants C_{RV} in (21). The internodal distance is set to $h = 0.005$ (corresponds to $N = 39504$ unknowns), polynomial degree $p = 3$ is used to construct the stencil-based interpolation problems

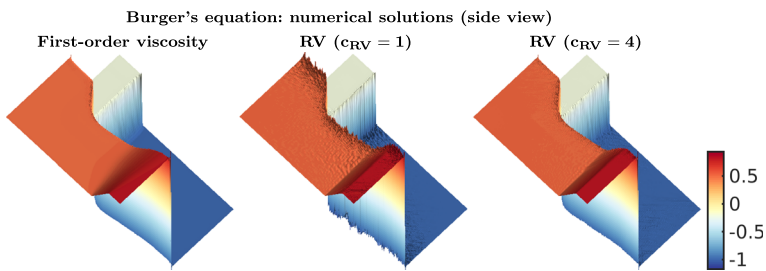


Fig. 14 Numerical solutions to the Burger’s equations from a rotated perspective, when the oversampled RBF-FD discretization is shock-stabilized using first-order viscosity, and residual viscosity for two choices of constants c_{RV} in (21). The internodal distance is set to $h = 0.005$ (corresponds to $N = 39504$ unknowns), polynomial degree $p = 3$ is used to construct the stencil-based interpolation problems

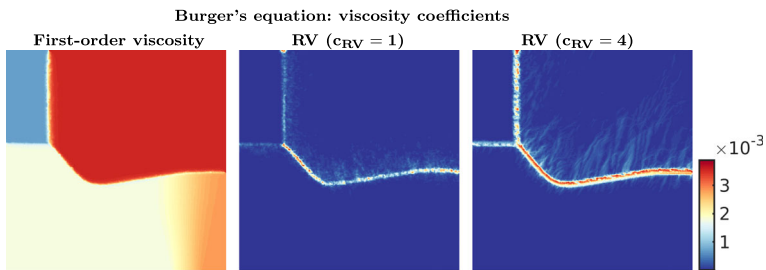


Fig. 15 Spatial variation of the viscosity coefficients, when the oversampled RBF-FD discretization is shock-stabilized using first-order viscosity, and residual viscosity for two choices of constants c_{RV} in (21). The internodal distance is set to $h = 0.005$ (corresponds to $N = 39504$ unknowns), polynomial degree $p = 3$ is used to construct the stencil-based interpolation problems

In Figs. 16 and 17, we display the convergence under node refinement, in 2-norm and 1-norm respectively, where the norms are defined in (32). The optimal convergence rates are expected to be 0.5 and 1. The convergence trends in all stabilized cases are close to these optimal rates. When stabilizing the scheme using the first-order viscosity, the error is constant-wise larger compared to when stabilizing the scheme using RV. We do not observe that an increase of p would—in the present case—lead to a significant improvement of the error by means of a constant.

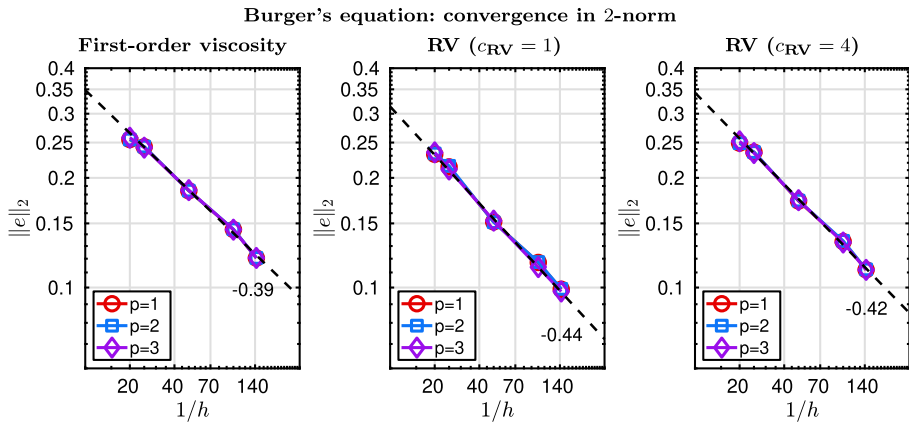


Fig. 16 Convergence in 2-norm, under node refinement for different choices of the monomial basis degree p , used to construct the stencil-based approximants. The convergence plots are displayed for cases when the oversampled RBF-FD is shock-stabilized using first-order viscosity and the residual viscosity

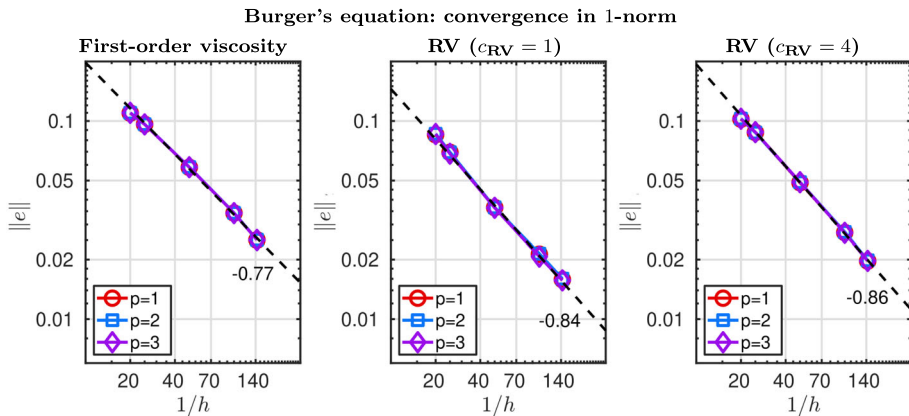


Fig. 17 Convergence in 1-norm, under node refinement for different choices of the monomial basis degree p , used to construct the stencil-based approximants. The convergence plots are displayed for cases when the oversampled RBF-FD is shock-stabilized using first-order viscosity and the residual viscosity

6 Numerical Study III: The Kurganov–Petrova–Popov Rotating Wave Problem

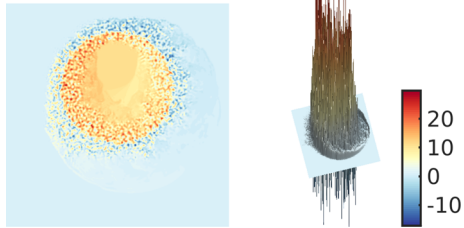
We solve another scalar conservation law with a nonlinear flux: the Kurganov–Petrova–Popov (KPP) problem, initially introduced in [13]. The flux is given by $F(u) = (\sin u, \cos u)$. The computational domain is a square $\Omega = [-2, 1.5] \times [2, 2.5]$. The initial condition and the Dirichlet boundary condition are in the same order defined as:

$$u(y, 0) = \begin{cases} \frac{14\pi}{4} & \text{if } \sqrt{y_1^2 + y_2^2} \leq 1 \\ \frac{\pi}{4} & \text{otherwise.} \end{cases}, \quad u(y, t)|_{\partial\Omega} = \frac{\pi}{4}. \tag{37}$$

We use the monomial basis degree $p = 3$ to construct the stencil based approximations, on a scattered point set X with a mean internodal distance $h = 0.02$ (corresponding to 39498

Fig. 18 Solution to the Kurganov–Petrova–Popov problem, when no shock stabilization is added to the oversampled RBF-FD discretization. The hyperviscosity term in (11) is active in order to stabilize the numerical scheme in time

The KPP problem: unstabilized numerical solutions



The KPP problem: stabilized numerical solutions

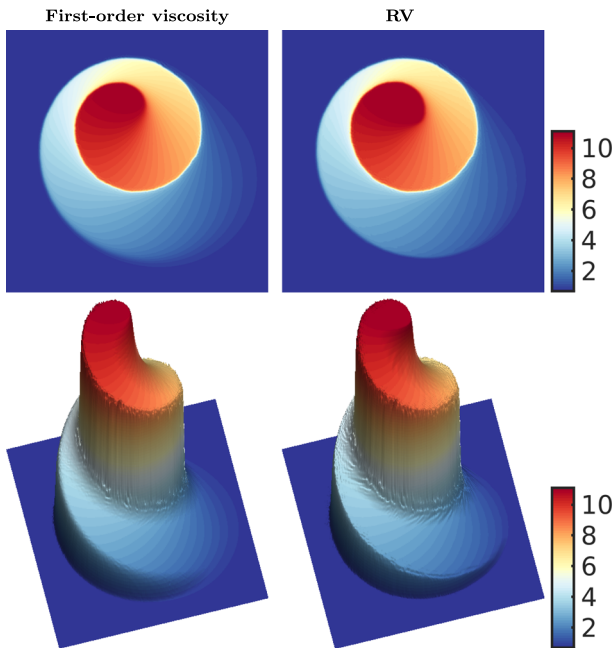


Fig. 19 A numerical solution to the Kurganov–Petrova–Popov problem from a top perspective (first row) and a side perspective (second row), when two different shock stabilizations are added to the oversampled RBF-FD discretization. The hyperviscosity term in (11) is active in addition, in order to stabilize the numerical scheme in time

nodes). The point set is obtained using the algorithm introduced in [6]. The oversampling parameter is set to $q = 5$ and the RV constant to $C_{RV} = 3$. We run the simulation until time $t = 1$ with the CFL number 0.2. Since the velocity field is for this benchmark rotational we use a fixed time step Δt , computed according to (31).

The solution at $t = 1$ when the shocks are not stabilized is displayed in Fig. 18, where we see oscillations so large, that the solution can not be seen as physical.

Stabilized solutions are displayed in Fig. 19. The solutions stabilized with the first-order viscosity and the residual viscosity are in an overall sense similar. A closer look, however, reveals that the residual viscosity solution includes sharper details along the edge of the spiral. The RV solution is less diffused compared to the first-order viscosity solution.

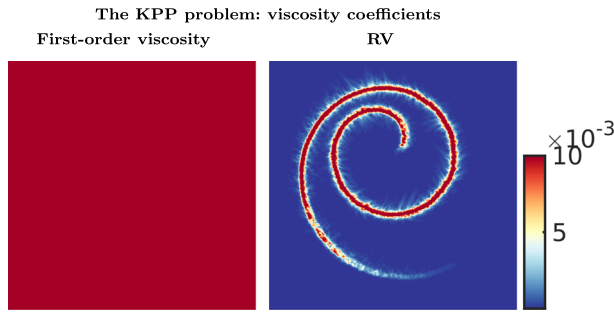


Fig. 20 The images display the spatial variation of the viscosity coefficient when using the first-order viscosity and the residual viscosity

The viscosity coefficients are given in Fig. 20, where we see that the residual viscosity is, roughly speaking, only active in the region of the discontinuity.

7 Numerical Study IV: Compressible Euler Equations

In this section we solve compressible Euler equations discretized in (17). The Euler system can be seen as a limiting case of the Navier-Stokes system of equations, when the physical viscosity term tends to 0. We solve several benchmarks which model a fluid in the state of a compressed gas. For all experiments we use the adiabatic constant $C_{ad} = 1.4$. The variable time steps for all considered cases are computed according to the formula:

$$\Delta t = CFL \min_{x_i \in X} \left[\frac{h_{loc}(x_i)}{\sqrt{v_1^2(x_i, t) + v_2^2(x_i, t) + C_{ad} p(x_i, t) / \rho(x_i, t)}} \right], \tag{38}$$

where h_{loc} is defined within the context of (21). The approximation errors for each unknown function are computed analogously to (32).

7.1 Sod’s Shock Tube Problem

The computational domain is a rectangle $\Omega = [0, 1] \times [0, 0.4]$, in which two fluids with different physical properties are separated by a membrane positioned at $y_1 = 0.5$. The initial condition is given by:

$$\begin{aligned} y_1 < 0.5 : \quad & \rho = 1, \quad \mathbf{v} = (0, 0), \quad p = 1, \\ y_1 > 0.5 : \quad & \rho = 0.125, \quad \mathbf{v} = (0, 0), \quad p = 0.1. \end{aligned} \tag{39}$$

The simulation of the two fluids is started by removing the membrane at $t = 0$, the final state is observed at $t = 0.25$. The boundary condition is *slip* ($\mathbf{v} \cdot \mathbf{n} = 0$) along all boundaries of the rectangle, where \mathbf{n} is the outward pointing normal.

We use scattered nodes generated using an algorithm from [6] to discretize Ω . Throughout the section, the CFL condition is set to 0.2, the oversampling parameter is set to $q = 5$ and the monomial basis degree to $p = 3$, if not stated otherwise.

The numerical solution (density), obtained using the RV stabilized oversampled RBF-FD method, is displayed in Fig. 21. We observe that the shock discontinuity and the contact

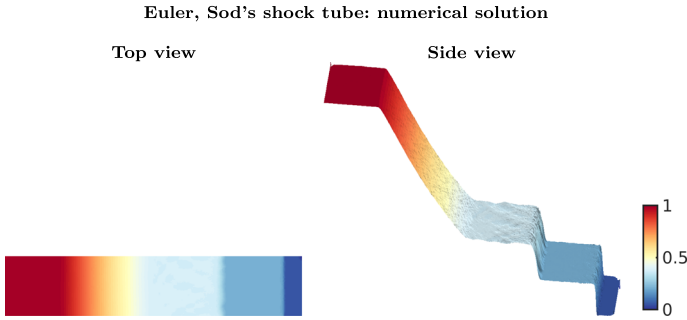


Fig. 21 The numerical solution (density ρ) of Sod's shock tube problem at $t = 0.25$, computed using the oversampled RBF-FD method. The internodal distance is set to $h = 0.003$ (corresponds to $N = 22244$ unknowns). The monomial basis degree used to construct the stencil-based approximants is $p = 3$. The oversampling parameter is set to $q = 5$

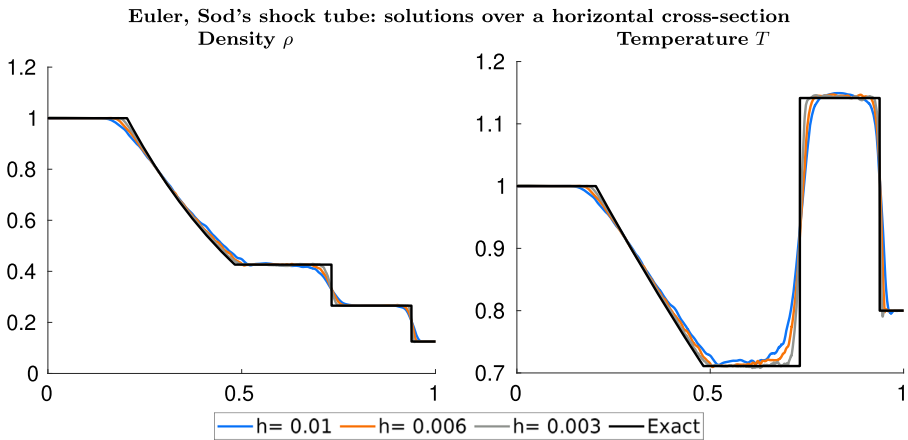


Fig. 22 A slice of the solution of Sod's shock tube problem at $t = 0.25$, computed using the oversampled RBF-FD method. The numerical solutions for different h are compared with the exact solution. The monomial basis degree used to construct the stencil-based approximants is $p = 3$. The oversampling parameter is set to $q = 5$

discontinuity are well captured. The mean distance between the computational nodes is set to $h = 0.003$ ($N = 22244$ unknowns).

Now we compare the RV stabilized RBF-FD solution with the exact solution. The exact solution is obtained for an equivalent problem in one dimension. We interpolate the 2-dimensional RBF-FD solution along the line $y_2 = 0.2$ in order to obtain an approximate 1-dimensional solution. This can be done since the variation of the 2-dimensional solution in the y_2 direction is very small. The first result is displayed in Fig. 22, where we show exact and numerical profiles of the density and the temperature. We observe that the discontinuous exact solution is well approximated by the numerical solution, and that the approximation gets increasingly better with a decreasing h .

In Fig. 23 we plot the 2-norm convergence of the numerical solution along the line $y_2 = 0.2$, where the exact 1D solution is taken as a reference. The optimal convergence rates for this norm are expected to be 0.5. For the density and the momentum, our convergence rates are optimal, while the convergence rate for the total energy is slightly higher than optimal. We

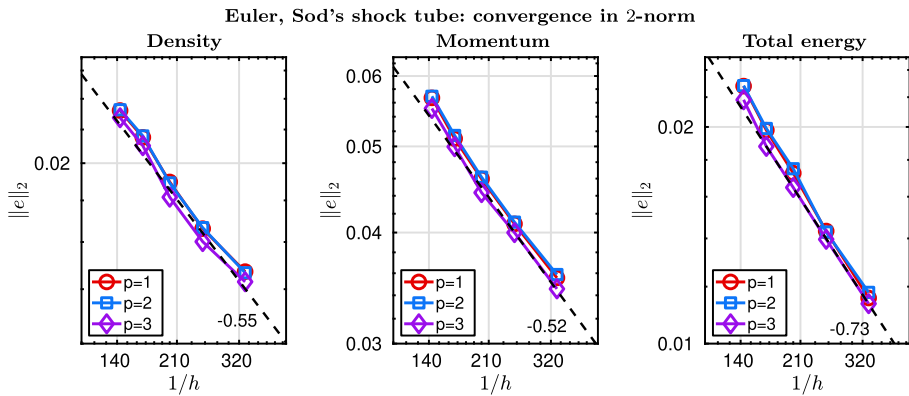


Fig. 23 Convergence in 2-norm under node refinement, for different choices of the monomial basis degree p , used to construct the stencil-based approximants

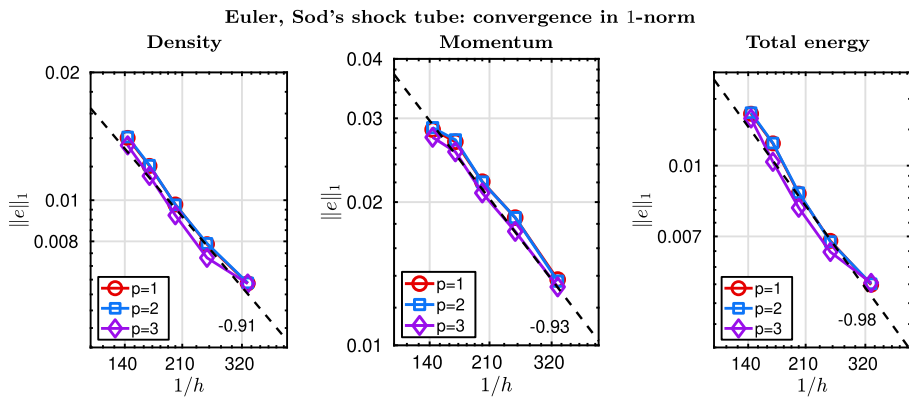


Fig. 24 Convergence in 1-norm under node refinement, for different choices of the monomial basis degree p , used to construct the stencil-based approximants

also observe that for the density, the approximation error in $p = 3$ case is slightly smaller compared to $p = 2$ and $p = 1$.

In Fig. 24 we show an analogous convergence plot, but in 1-norm. Here the optimal convergence rate is 1. The convergence plots in all cases are close to the optimum. An increase in p gives a slight improvement of the approximation error by means of a constant.

In [19], the authors used the RV stabilized finite element method to solve Sod's shock tube problem using the same set of physical parameters. Comparing Figs. 23 and 24 from the present paper, with Figure 6 from [19], we can observe that the errors in 2-norm and 1-norm are comparable in magnitude and the slopes.

7.2 A 2D Riemann Problem

The domain is a square $\Omega = [0, 1] \times [0, 1]$. The initial condition is defined such that it takes different values in different quadrants of the square:

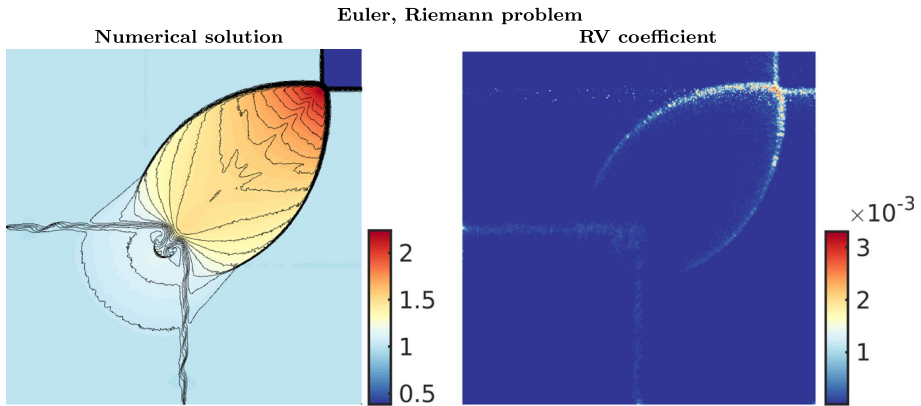


Fig. 25 The numerical solution of the Riemann problem, together with the spatial distribution of the residual viscosity coefficient. The colormap of the numerical solution shows the pressure in the interval $[0.37, 2.23]$, while the contour lines show the density in the interval $[0.54, 1.7]$

$$\begin{aligned}
 \rho &= 4/5, & p &= 1, & \mathbf{v} &= (0, 0), & \text{in } 0 < y_1 < 0.5, & 0 < y_2 < 0.5, \\
 \rho &= 1, & p &= 1, & \mathbf{v} &= (0.7276, 0), & \text{in } 0 < y_1 < 0.5, & 0.5 < y_2 < 1, \\
 \rho &= 1, & p &= 1, & \mathbf{v} &= (0, 0.7276), & \text{in } 0.5 < y_1 < 1, & 0 < y_2 < 0.5, \\
 \rho &= 17/32, & p &= 2/5, & \mathbf{v} &= (0, 0), & \text{in } 0.5 < y_1 < 1, & 0.5 < y_2 < 1.
 \end{aligned} \tag{40}$$

The boundary conditions are *slip* on the top side and the right side of the square domain. On the bottom and the left side of the square domain, we use the inflow Dirichlet boundary conditions. These are for all t set to the corresponding values of the initial condition. The scattered nodes over Ω are placed using the algorithm provided in [6]. We set the monomial basis degree to $p = 3$, the oversampling parameter to $q = 5$, the internodal distance to $h = 0.0025$ (corresponds to $N = 156981$ unknowns), the CFL number to 0.2 and the RV constant to $C_{RV} = 3$, and run the simulation until $t = 0.25$.

The result is given in Fig. 25, where we display the RBF-FD solution stabilized using RV and the corresponding spatial distribution of the viscosity coefficient. We observe that the solution is sharp around the shock in the upper right corner of the domain, and that the contact discontinuity in the lower left quadrant is well defined. Furthermore, the magnitude of the viscosity coefficient is largest in the shock region and slightly smaller in the region of the contact discontinuity. The solution looks very similar to the one obtained using the RV stabilized finite element method in Figure 7 of [19], and also to all of the solutions obtained using six different shock-capturing schemes in Figure 4.2 of [14].

7.3 A Channel Flow Over a Forward Facing Step

We study a Mach 3 supersonic flow over a forward facing step in a rectangular channel $\Omega = [0, 3] \times [0, 1]$. The sharp inward corner of the forward facing step is located at coordinate $(0.6, 0.2)$. The initial condition is: $\rho = 1.4$, $\mathbf{m} = (4.2, 0)$, $\mathcal{E} = 8.8$. We use slip boundary conditions on the top and the bottom boundaries of the channel. On the left boundary of the channel we use an inflow (Dirichlet) boundary condition, where for all t we prescribe the values of the initial condition. On the right side of the channel we mimic the outflow by not imposing any boundary conditions. We run the simulation until $t = 4$ using $N = 117432$

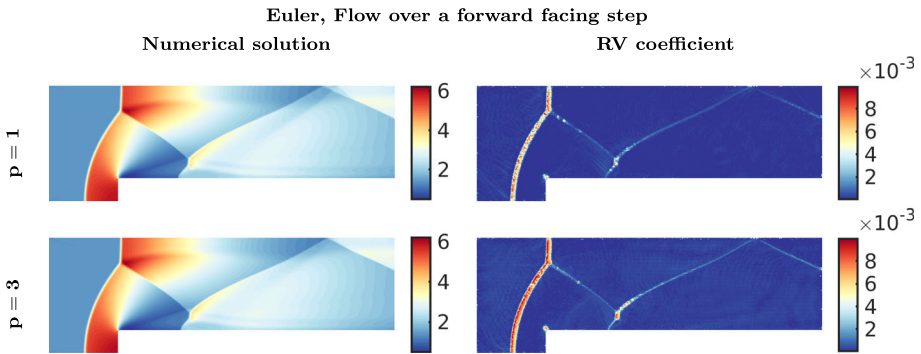


Fig. 26 The results are made using $N = 117432$ nodes. The numerical solution (left column) is given in terms of density ρ at $t = 4$, for two choices of a monomial basis degree p to construct the stencil based approximation. The plots in the right column are residual viscosity coefficients for the two choices of p

nodes obtained using Gmsh [8]. Other parameters are $C_{RV} = 5$, $CFL = 0.3$. We also consider two choices of monomial basis degrees: $p = 1$ and $p = 3$.

The flow entering the channel hits the step and then creates a bow shock that propagates towards the upper boundary, and then keeps reflecting between upper and lower boundaries. Close to the first reflection where the shocks meet, there is a so-called triple point. From the direction of the triple point towards the outflow, the physical solution has a contact discontinuity, which is challenging to capture in a numerical sense.

The numerical results are collected in Fig. 26. The numerical solutions for $p = 1$ and $p = 3$ are similar to the solutions displayed in Figure 9 of [19]. A prevailing difference is that the shock reflection close to the inward facing corner has a different location. This is ascribed to the fact that in this paper we do not smooth out the inward corner as the authors in [19] do, but keep it sharp. In our case, the contact discontinuity is captured for both choices of p . When $p = 1$ we notice that the solution around the reflection closest to the outflow of the channel, has a large error by means of the phase, compared to when using $p = 3$. This shows a benefit of using a high-order discretization, even if the underlying solution does not have a sufficient regularity to support the high-order convergence.

7.4 Explosion in a Domain with Cylinders

This problem was initially introduced in [19]. The computational domain is the disc with radius 2. In addition, the domain has eight inner circular boundaries with radius 0.3, which are placed at distance 1.4 from the origin. The distance between the neighboring inner circular boundaries are equal. The initial condition is a discontinuous function, where a compressed gas with $\rho = 1$, $p = 1$ is put inside the disc with radius $\sqrt{0.4}$, located at the origin. Outside of that disc we have $\rho = 0.125$ and $p = 1$. The velocity is $\mathbf{v} = (0, 0)$ throughout the domain. Slip boundary conditions are used for the exterior boundary and all of the interior boundaries. The simulation is run until $t = 4.25$.

We use $N = 337356$ nodes obtained using Gmsh [8]. Other parameters are: $p = 3$, $C_{RV} = 3$ and $CFL = 0.3$. The results are given in Fig. 27, where we observe that RV performs well, even in cases where the numerical solution exhibits small details. The spatial distribution of the residual viscosity coefficient is displayed in Fig. 28, where we see that the action of viscosity is localized.

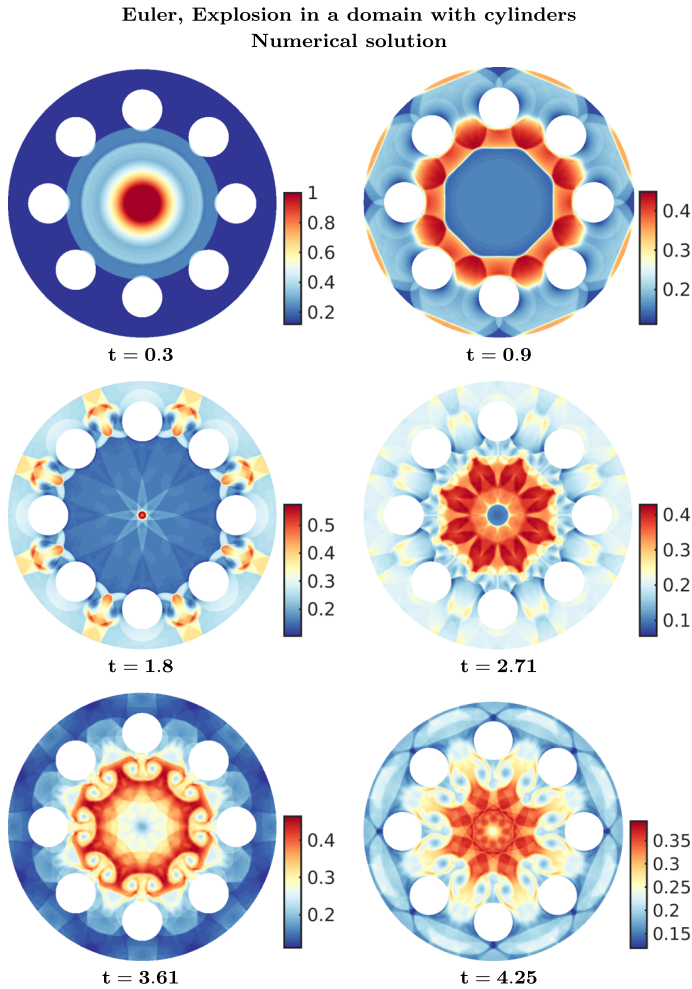


Fig. 27 Numerical solution of the benchmark Explosion in a domain with cylinders, at different points in time t . The solution is obtained using $N = 337356$ nodes. The oversampling parameter is $q = 5$. The polynomial degree used to construct the stencil-based approximation is $p = 3$

8 Final Discussion

In this paper we covered several aspects of discretizing conservation laws using the RBF-FD method.

We observed that oversampling by itself does not improve the time stability of the RBF-FD method. A theoretical argumentation for this behavior and further analysis is given in [27].

Another observation is that the collocation RBF-FD method is nearly as accurate as the oversampled RBF-FD method when using Dirichlet boundary conditions, which is in line with the observations made in [26]. As investigated in Sect. 4, the residual viscosity stabilization framework is applicable to both, the collocation setting and the oversampled setting of the RBF-FD method.

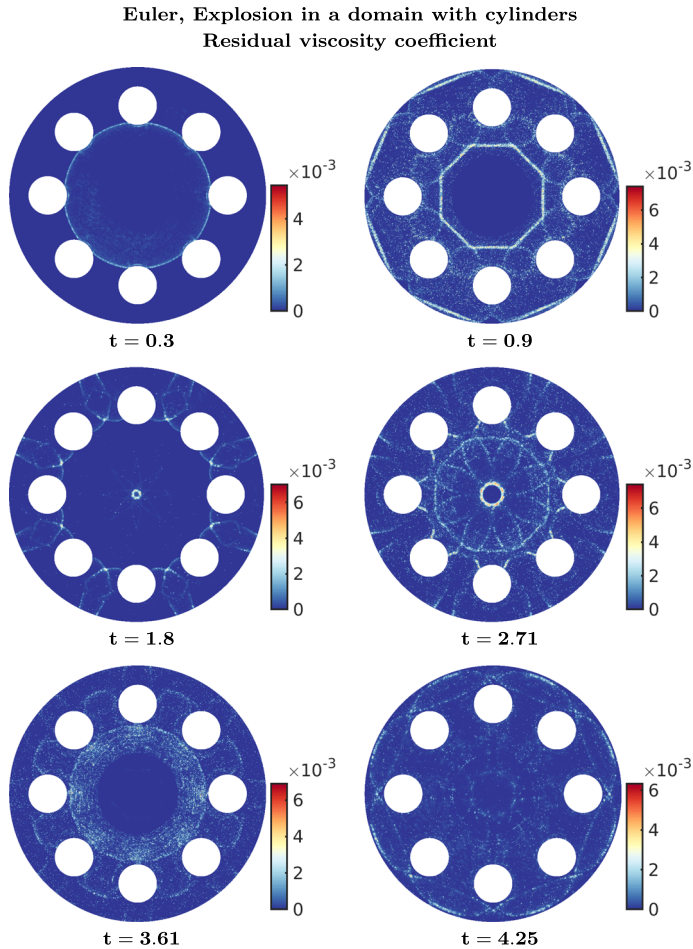


Fig. 28 Spatial distribution of the residual viscosity coefficient used to compute the solution of the benchmark Explosion in a domain with cylinders. The coefficient is displayed at different points in time t . The corresponding solution is computed obtained using $N = 337356$ nodes. The oversampling parameter is $q = 5$. The polynomial degree used to construct the stencil-based approximation is $p = 3$

The RV constant C_{RV} which is defined by the user is not a sensitive parameter. We did, however, notice that C_{RV} had to be chosen larger than 1, when the magnitude of the numerical solution was large. This was not observed when RV was combined with the finite element methods, for example in [19]. We did not fully explore the reasons behind that. A speculative explanation is that we used a different residual definition compared to the residual definition used in [19].

We found that a symmetric hyperviscosity operator (12) is an effective stabilization in time. The residual as defined in the present work turned out to be an excellent indicator of discontinuities. The residual viscosity stabilization (RV) is consistent when the solution is smooth.

Finally, all experiments confirmed that a combination of the RBF-FD method and the RV stabilization provides a robust framework for discretizing nonlinear conservation laws in scalar and system settings.

Acknowledgements We thank (in alphabetical order) Lukas Lundgren, Tuan Anh Dao and Vidar Stiernström from Uppsala University for fruitful discussions about time-dependent conservation laws. The computations were enabled by resources in project SNIC 2022/22-428 provided by the Swedish National Infrastructure for Computing (SNIC) at UPPMAX.

Funding Open access funding provided by Uppsala University.

Open Access This article is licensed under a Creative Commons Attribution 4.0 International License, which permits use, sharing, adaptation, distribution and reproduction in any medium or format, as long as you give appropriate credit to the original author(s) and the source, provide a link to the Creative Commons licence, and indicate if changes were made. The images or other third party material in this article are included in the article's Creative Commons licence, unless indicated otherwise in a credit line to the material. If material is not included in the article's Creative Commons licence and your intended use is not permitted by statutory regulation or exceeds the permitted use, you will need to obtain permission directly from the copyright holder. To view a copy of this licence, visit <http://creativecommons.org/licenses/by/4.0/>.

(Appendix) A High-Order Time Derivative Approximation

```
function w = timedderivatives (t)

    scale = 1/max(abs(t));
    t = t*scale;
    t_eval = t(end);

    A = zeros(size(t,1), size(t,1));
    b_t = zeros(1, size(t,1));
    for k=1:length(t)
        A(:,k) = t.^(k-1);
        b_t(k) = (k-1)*t_eval.^(k-2);
    end
    w = scale*(b_t*inv(A));

end
```

References

1. Barnett, G.A.: A robust RBF-FD formulation based on polyharmonic splines and polynomials. Ph.D. thesis, University of Colorado at Boulder, Dept. of Applied Mathematics, Boulder, CO, USA (2015)
2. Bayona, V.: An insight into RBF-FD approximations augmented with polynomials. *Comput. Math. Appl.* **77**, 2337–2353 (2019). <https://doi.org/10.1016/j.camwa.2018.12.029>
3. Bayona, V., Flyer, N., Fornberg, B., Barnett, G.A.: On the role of polynomials in RBF-FD approximations: II. Numerical solution of elliptic PDEs. *J. Comput. Phys.* **332**, 257–273 (2017). <https://doi.org/10.1016/j.jcp.2016.12.008>
4. Flyer, N., Fornberg, B., Bayona, V., Barnett, G.A.: On the role of polynomials in RBF-FD approximations: I. Interpolation and accuracy. *J. Comput. Phys.* **321**, 21–38 (2016). <https://doi.org/10.1016/j.jcp.2016.05.026>
5. Flyer, N., Lehto, E., Blaise, S., Wright, G.B., St-Cyr, A.: A guide to RBF-generated finite differences for nonlinear transport: shallow water simulations on a sphere. *J. Comput. Phys.* **231**(11), 4078–4095 (2012). <https://doi.org/10.1016/j.jcp.2012.01.028>
6. Fornberg, B., Flyer, N.: Fast generation of 2-D node distributions for mesh-free PDE discretizations. *Comput. Math. Appl.* **69**(7), 531–544 (2015). <https://doi.org/10.1016/j.camwa.2015.01.009>

7. Fornberg, B., Lehto, E.: Stabilization of RBF-generated finite difference methods for convective PDEs. *J. Comput. Phys.* **230**(6), 2270–2285 (2011). <https://doi.org/10.1016/j.jcp.2010.12.014>
8. Geuzaine, C., Remacle, J.F.: Gmsh: a 3-D finite element mesh generator with built-in pre- and post-processing facilities. *Int. J. Numer. Methods Eng.* **79**(11), 1309–1331 (2009). <https://doi.org/10.1002/nme.2579>
9. Guermond, J.L., Pasquetti, R., Popov, B.: Entropy viscosity method for nonlinear conservation laws. *J. Comput. Phys.* **230**(11), 4248–4267 (2011). <https://doi.org/10.1016/j.jcp.2010.11.043>
10. Hughes, T.J.R., Scovazzi, G., Tezduyar, T.E.: Stabilized methods for compressible flows. *J. Sci. Comput.* **43**(3), 343–368 (2010). <https://doi.org/10.1007/s10915-008-9233-5>
11. Jančič, M., Slak, J., Kosec, G.: Monomial augmentation guidelines for RBF-FD from accuracy versus computational time perspective. *J. Sci. Comput.* **87**(1), Paper No. 9, 18 (2021). <https://doi.org/10.1007/s10915-020-01401-y>
12. Johnson, C., Szepessy, A., Hansbo, P.: On the convergence of shock-capturing streamline diffusion finite element methods for hyperbolic conservation laws. *Math. Comput.* **54**(189), 107–129 (1990). <https://doi.org/10.2307/2008684>
13. Kurganov, A., Petrova, G., Popov, B.: Adaptive semidiscrete central-upwind schemes for nonconvex hyperbolic conservation laws. *SIAM J. Sci. Comput.* **29**(6), 2381–2401 (2007). <https://doi.org/10.1137/040614189>
14. Liska, R., Wendroff, B.: Comparison of several difference schemes on 1D and 2D test problems for the Euler equations. *SIAM J. Sci. Comput.* **25**(3), 995–1017 (2003). <https://doi.org/10.1137/S1064827502402120>
15. Lu, L., Nazarov, M., Fischer, P.: Nonlinear artificial viscosity for spectral element methods. *C. R. Math. Acad. Sci. Paris* **357**(7), 646–654 (2019). <https://doi.org/10.1016/j.crma.2019.07.006>
16. Marras, S., Nazarov, M., Giraldo, F.X.: Stabilized high-order Galerkin methods based on a parameter-free dynamic SGS model for LES. *J. Comput. Phys.* **301**, 77–101 (2015). <https://doi.org/10.1016/j.jcp.2015.07.034>
17. Nazarov, M.: Convergence of a residual based artificial viscosity finite element method. *Comput. Math. Appl.* **65**(4), 616–626 (2013). <https://doi.org/10.1016/j.camwa.2012.11.003>
18. Nazarov, M., Hoffman, J.: Residual-based artificial viscosity for simulation of turbulent compressible flow using adaptive finite element methods. *Int. J. Numer. Methods Fluids* **71**(3), 339–357 (2013). <https://doi.org/10.1002/fld.3663>
19. Nazarov, M., Larcher, A.: Numerical investigation of a viscous regularization of the Euler equations by entropy viscosity. *Comput. Methods Appl. Mech. Eng.* **317**, 128–152 (2017). <https://doi.org/10.1016/j.cma.2016.12.010>
20. Persson, P.O., Strang, G.: A simple mesh generator in Matlab. *SIAM Rev.* **46**(2), 329–345 (2004). <https://doi.org/10.1137/S0036144503429121>
21. Shankar, V., Fogelson, A.L.: Hyperviscosity-based stabilization for radial basis function-finite difference (RBF-FD) discretizations of advection-diffusion equations. *J. Comput. Phys.* **372**, 616–639 (2018). <https://doi.org/10.1016/j.jcp.2018.06.036>
22. Shankar, V., Wright, G.B., Narayan, A.: A robust hyperviscosity formulation for stable RBF-FD discretizations of advection–diffusion–reaction equations on manifolds. *SIAM J. Sci. Comput.* **42**(4), A2371–A2401 (2020). <https://doi.org/10.1137/19M1288747>
23. Stiernström, V., Lundgren, L., Nazarov, M., Mattsson, K.: A residual-based artificial viscosity finite difference method for scalar conservation laws. *J. Comput. Phys.* **430**, 110100 (2021). <https://doi.org/10.1016/j.jcp.2020.110100>
24. Tominec, I.: Rectangular and square RBF-FD matrices in MATLAB. <https://github.com/IgorTo/rbf-fd> (2021). <https://doi.org/10.5281/zenodo.4525550>
25. Tominec, I., Breznik, E.: An unfitted RBF-FD method in a least-squares setting for elliptic PDEs on complex geometries. *J. Comput. Phys.* **436**, Paper No. 110283, 24 (2021). <https://doi.org/10.1016/j.jcp.2021.110283>
26. Tominec, I., Larsson, E., Heryudono, A.: A least squares radial basis function finite difference method with improved stability properties. *SIAM J. Sci. Comput.* **43**(2), A1441–A1471 (2021). <https://doi.org/10.1137/20M1320079>
27. Tominec, I., Nazarov, M., Larsson, E.: Stability estimates for radial basis function methods applied to time-dependent hyperbolic pdes. *arXiv preprint arXiv:2110.14548* (2021)
28. Tominec, I., Villard, P.F., Larsson, E., Bayona, V., Cacciani, N.: An unfitted radial basis function generated finite difference method applied to thoracic diaphragm simulations (2021)
29. Von Neumann, J., Richtmyer, R.D.: A method for the numerical calculation of hydrodynamic shocks. *J. Appl. Phys.* **21**, 232–237 (1950)

Publisher's Note Springer Nature remains neutral with regard to jurisdictional claims in published maps and institutional affiliations.